

**CHARACTERIZATION OF BRAIN SURFACE STRAINS DURING
CONTROLLED CORTICAL IMPACT**

by

Huijae Kim

A thesis submitted to the faculty of
The University of Utah
in partial fulfillment of the requirements for the degree of

Master of Science

Department of Mechanical Engineering

The University of Utah

May 2015

Copyright © Huijae Kim 2015

All Rights Reserved

ABSTRACT

Traumatic brain injury is a devastating medical problem worldwide. Contusion, which involves direct damage of both brain tissue and surrounding blood vessels, has been called the hallmark of head injury. Controlled cortical impact (CCI) is a commonly used experimental model to study contusion and may be useful in the study of vascular injury, but there is currently no way to measure strain in the cortex or in the cortical blood vessels. Finite element (FE) models have been utilized to characterize the deformation of brain tissue during CCI, but none have explored strains relevant to the blood vessels. Specifically, these models have reported strains relative to the global reference frame only. The objective of this research was to characterize strains tangent to the surface of the cortex in order to estimate deformations that vessels on the surface of the brain may experience during CCI. An FE model was built from coronal section images of a mouse brain. The brain, pia-arachnoid complex, dura, and skull were separately modeled along with a rigid indenter. Global strains were transformed to the local coordinate system defined by the orientation of the brain surface at the point of interest. Strain distributions were investigated in the baseline model and showed that circumferential strain is the primary contributor to principal strain, while radial strain is high in the center but contributes little to tensile strains away from the very center. In order to characterize the influence of experimental parameters on predicted deformations, indentation rate, depth, craniotomy size, indentation angle, and indenter tip shape were each varied, and the

resulting strain distribution was compared to the baseline results. Tip shape was the most influential parameter, producing the highest strain concentration on the surface of the brain. Indentation depth, rate, and angle also significantly influenced the strain distribution on the brain. Based on previously reported values of failure strain for cerebral arteries, simulations consistently predicted the occurrence of vessel injury, a frequent outcome of CCI.

CONTENTS

ABSTRACT.....	iii
Chapters	
1 INTRODUCTION.....	1
1.1 Traumatic Brain Injury.....	1
1.2 Contusion and Controlled Cortical Impact.....	2
1.3 Geometry of Cerebral Blood Vessels.....	3
1.4 Literature Review of FE CCI Rat Brain Model.....	4
1.5 Objective.....	5
2 METHODS.....	7
2.1 Base Model.....	7
2.2 Influence of Ventricles.....	11
2.3 Element Types.....	15
2.4 Transformation of Strains.....	17
2.5 Parameter Study.....	21
3 RESULTS.....	36
3.1 Base Model.....	36
3.2 Influence of Indentation Rate.....	38
3.3 Influence of Indentation Depth.....	39
3.4 Influence of the Craniotomy Size.....	40
3.5 Influence of Indenter Angle.....	40
3.6 Influence of Indenter Tip Shape.....	41
4 DISCUSSION.....	56
5 CONCLUSION AND FUTURE WORK.....	61
Appendices	
A FINITE ELEMENT CODE.....	63

B MATLAB CODE.....	69
REFERENCES.....	75

CHAPTER 1

INTRODUCTION

1.1 Traumatic Brain Injury

Traumatic brain injury (TBI) is a serious problem in the United States and Europe [1,2]. About 1 million people per year visit hospitals due to TBI in Europe [2], and about 1.7 million people suffered with TBI each year in the U.S. [1]. Three percent of 1.7 million people died, and TBI is the main reason of death and disability [1-3]. Those who suffer TBI commonly experience deficits such as impaired sensation, consciousness, or memory. These effects might be temporary or permanent [1,6]. TBI can be caused by a direct impact on the skull with an object, through blast waves, or through contact between the brain and skull caused by rapid acceleration or deceleration [1,3]. The leading cause of TBI is falls, and rates are highest for children aged 4 years and less and adults aged 75 years and older. Motor vehicle accidents are the leading causes of death related to TBI, and rates are highest for adults aged 20 to 24 years [1,4]. Brain injuries can be categorized into two injuries: focal injury and diffuse injury [5,7]. Focal injury is caused by contact and includes contusion on the brain and intracranial hemorrhage. Diffuse brain injury is due to rapid acceleration or deceleration and includes axonal injury and brain swelling [5]. TBI is not limited to the moment of exposure to the external force. Primary injury occurs at the moment of injury and results in contusion, hemorrhage, and damage to tissues. Secondary injury develops over time from the primary injury [5,6]. There have

been many studies of TBI, but injury mechanisms of TBI are not well defined. It is difficult to predict the outcome, and it is not clear if the results between persons will be similar under the same conditions. Given the current state of knowledge, complete prevention of TBI is not possible since the cause is not well defined [3,7,8,27].

1.2 Contusion and Controlled Cortical Impact

Contusion has been called the hallmark of TBI [9,10,12]. Contusion is a bruise on the brain surface and includes hemorrhage and less severe breakdown of the blood-brain barrier. Contusions usually appear near the area of external impact or in regions of the brain adjacent to protruding structures of the inner skull. Contusions also commonly appear on the side of the brain opposite from the impact, which are called countercoup injuries [13]. Contusions may develop, or increase in size over time. The exact mechanisms of contusion and associated vessel leakage are not well defined [10–12].

Controlled cortical impact (CCI) is a direct deformation animal model that is widely used to create experimental contusion. In a CCI experiment, a small section of the skull is removed and an indenter strikes the dura mater directly. The advantages of CCI are that loading parameters such as indenter velocity and size and impact depth can be clearly controlled. CCI creates focal injury, which due to the well-controlled-parameters is considered by many to be a good model to study contusion despite the fact that force is not transmitted through the skull as is usually the case in TBI.

There are two operating type of CCI: pneumatic and electromagnetic devices. In our lab, an electromagnetic device, with a 3.25 mm diameter hemispherical tip, is used. The indenter strikes the exposed dura through the craniotomy. After a determined survival time, the animal is sacrificed, and the brain is removed. Brain tissues in the region of

injury are sliced and examined with immunohistological techniques to inspect the scope of damage. Immunoglobulin G (IgG) is a plasma protein that is used to study the damage to the blood-brain barrier (BBB) [10]. While CCI effectively produces contusion, it is not currently possible to observe the tissue and blood vessel deformation and injury. Thus, there is no way to measure strains in cortex. Bayly et al. [15] used a Magnetic Resonance Imaging (MRI) to observe *in vivo* brain deformations during CCI in the rat and was able to calculate strain fields on the brain. However, due to the relatively low sample rates (Hz), the observed strains might be underestimated. Strains associated with regions where damage results from repeated impacts are clearly also not reliable. Despite the widespread use of CCI, little is known about the details of the associated vascular injury.

1.3 Geometry of Cerebral Blood Vessels

The brain takes about 15 to 20% of the blood from the heart, while it accounts for just 2% of the total body weight [14]. There is a dense network of blood vessels in the brain, but the response of the vessels to trauma is not well defined. Understanding the geometry of cerebral blood vessels is necessary to study the effects of TBI, such as the rupture of blood vessels.

There are four main arteries that deliver blood to the brain: the right and left internal carotid and the right and left vertebral arteries. The internal carotid arteries provide blood to the anterior cerebrum, and the vertebral arteries support the posterior of the cerebrum, cerebellum, and the brain stem. The internal carotid and basilar arteries meet at the base of the brain and form the Circle of Willis, providing redundancy of flow if one of the supplying arteries is impaired. Blood from the Circle of Willis travels along the surface of the brain after being divided into six primary arteries. These arteries then divide into

smaller arteries to cover the surface of the cortex. Smaller branches from the surface of the brain penetrate into the brain cortex and provide blood and nutrition to the brain tissue. In the cerebral venous system, there are two categories of valveless veins: the superficial cortical veins and the deep or central veins. The superficial cortical veins are on the surface of the brain and draw blood from the cerebral cortex and subcortical white matter. The deep or central veins group draws blood from the deep brain [14].

1.4 Literature Review of FE CCI Rat Brain Model

Many species of animals have been used in experiments to study TBI, including rodents. The history of FE modeling of the animal brain is relatively short, but it is clear that both experiment and computational analysis should be developed together to provide better understanding of the mechanisms of TBI. There are many publications related to FE animal brain models, including those investigating CCI results in the rat.

Pena et al. [11] developed a 2D FE rat brain model to study CCI. There were no meninges or skull in the model, so it included just the brain and the piston. Three different elasticity (constant, inverse linear, and linear) were used for brain tissue as a parameter study, and the brain was meshed with tetrahedral elements. The piston directly struck the brain. Tissue displacement, mean stress, and shear stress were observed to compare the results from experiments.

Mao [7] built a 3D FE rat model to study CCI. It included the skull, brain, and meninges such as dura and pia-arachnoid complex (PAC). Brain structures such as the cortex, corpus callosum, hippocampus, ventricles, thalamus, and hypothalamus were also separately modeled. The brain was built as a homogeneous, isotropic, and viscoelastic structure, and meshed with hexahedral elements. The skull was built as a rigid structure,

and there was a craniotomy on the skull. The negative pressure or the indentation applied on the exposed dura. Intracranial pressure (ICP) and maximum principal strain (MPS) were observed.

Mathur [23] built a 3D FE mouse model to study CCI. The model included skull, meninges such as dura and pia-arachnoid complex (PAC), and brain. Ventricles were not considered in this model. The brain was built as a homogeneous, isotropic, and viscoelastic structure, and meshed with hexahedral elements. The skull was built as a rigid structure, and there was a craniotomy on the skull. A piston directly struck the exposed dura through the craniotomy. Green-Lagrange first principal strain, logarithmic first principal strain-rate, and effective stress were observed.

1.5 Objective

Contusion is common following TBI. Contusion includes hemorrhage and other vascular leakage. The exact mechanisms of contusion are not well defined. CCI is considered as a good model to study TBI, but the study of *in vivo* vascular injury is limited. Specifically, there is no particular way to measure strains in the cortex; therefore, it is challenging to study damage of blood vessels in the region. FE modeling can be used to estimate deformations of the cortex. Defining strain in the cortex can help clarify cerebral vessel mechanics. Blood vessels reside on the brain surface and penetrate into the brain. Given the variable orientation of the vessels in the deep brain and the well-ordered orientation of the vessels on the brain surface (i.e, they lie within a plane tangent to the brain surface), the surface of the brain is good place to observe strains to study vascular injury. A number of FE analyses have been performed to study contusion, but results have been reported in a global reference frame that generally does not correspond

with vessel orientation. A local coordinate system can be used to determine relevant strains. The 3D mouse brain model in this research was built as an extension of the Mathur [23] model. The objective of this research was to use an improved version of this model to characterize strains experienced by blood vessels on the surface of the cerebral cortex during controlled cortical impact. Strains were explored as a function of parameters that are experimentally variable to help guide future animal modeling.

CHAPTER 2

METHODS

This chapter describes the development of an anatomically detailed FE mouse brain model to study brain tissue response under CCI. Building on the model previously reported by Mathur [23], the potential influence of the ventricles on cortical deformations was considered. Additionally, strains were converted from global coordinates to a local coordinate system aligned with the surface of the brain. The resulting strains were explored as a function of various model parameters.

2.1 Base Model

An FE model was built from coronal section images of a mouse brain. The brain, pia-arachnoid complex, dura, and skull were separately modeled, along with a rigid indenter. The contacts, material properties, and convergence study are included in this section.

2.1.1 Geometry and Mesh

Hexahedral elements were used for 3D mouse brain. Meninges, including pia-arachnoid complex (PAC) and dura, were built from the brain elements. The model was composed of a total of 678,363 elements. The brain had 429,318 elements, PAC and dura had 27,864 shell elements, and the rest of the elements were the indenter and skull.

2.1.1.1 Mouse Brain

It is necessary to have accurate geometry to obtain realistic results from an FE model. The mouse brain geometry was built from scanned images of coronal sections of the brain. The scanned images were obtained from an online database (Mouse Brain Library; http://www.mbl.org/atlas170/atlas170_frame.html). A total of 37 brain section images of a 51-day-old C57BL/6J male mouse, with a body weight of 20.2 gm and a brain weight of 477 mg, were used to create the geometry [19].

The geometry of the brain was built using ImageJ (National Institutes of Health, Bethesda, MD) and SolidWorks (SolidWorks, Waltham, MA). Boundaries of relevant brain structures were first digitized using ImageJ (National Institutes of Health, Bethesda, MD), and the coordinates of the digitized points were exported in text format. The list of coordinates was then imported into SolidWorks (SolidWorks, Waltham, MA) and contour lines were created using the “XYZ curves” option. The contour lines were then connected to each other and converted into a solid using the “Boundary Boss/Base” option. Figure 2.1 shows 3D mouse brain model.

2.1.1.2 Meninges and Skull

The solid model built with SolidWorks was imported into HyperMesh (Altair Engineering, Troy, MI) for meshing and to create the meninges and skull. First-order hexahedral elements were used for this model. Hexahedral elements were widely used in previous papers about computational brain models [7]. Further discussion about different element types will be discussed in section 2.2.4. In the living system, the pia mater is attached to the brain and the dura is attached to the inner surface of the skull. The arachnoid mater is located between the pia and the dura. Arachnoid trabeculae are located

in the subarachnoid space and are attached to the pia layer and the arachnoid layer. The arachnoid trabeculae form complex networks in the subarachnoid space. Their profile is 5 to 7 μm , and their orientations are completely random. Due to the complex structure and small profile of the subarachnoid space, as well as the cerebrospinal fluid contained within it, it is difficult to build the detailed subarachnoid layer in a 3D brain model. Instead, the pia and the arachnoid layers were thus modeled as one layer, the pia-arachnoid complex (PAC), similar to Mao et al. [7]. Since the PAC is attached to the brain, it is necessary that it follow the profile of the brain surface. The “FACES” option in HyperMesh was used to create a layer of shell elements just exterior to the outer layer of solid elements in the brain to represent the PAC. Membrane elements would likely be more appropriate here, but the “FACES” option can only generate shell elements. Mao et al. also treated membranes as a single layer of shell elements. Shell elements with such a small thickness have little resistance to bending. The dura layer was created by copying the pia-arachnoid and offsetting to account for the thickness of the pia-arachnoid. The thicknesses of the dura and pia-arachnoid were designated 20 microns and 15 microns, respectively, in LS-Dyna. One additional layer was created outside the dura to represent the skull. The skull was designed as a rigid part.

2.1.2 Contacts

LS-Dyna was used as the finite element method (FEM) solver. It suits simulations that analyze large deformations at high rates. Explicit time integration was used as the main solution methodology for this model. One node at the bottom of the skull was fixed to constrain the motion of the skull. The other parts were allowed to move freely within the skull. “AUTOMATIC_SURFACE_TO_SURFACE” contact was used to define

friction contacts between dura and the skull, dura and the piston, and dura and PAC [24]. A friction coefficient of 0.2 was used [7].

2.1.3 Material Properties

A Kelvin Maxwell Viscoelastic material was used for the brain tissue. The theoretical equation for the material is described by

$$G(t) = G_{\infty} + (G_0 - G_{\infty})e^{-\beta t} \quad (2.1)$$

G_0 is the instantaneous shear modulus

G_{∞} is the long term shear modulus

β is the decay constant.

The brain is considered homogeneous, isotropic, and nearly incompressible. The real brain is anisotropic and inhomogeneous, but in this simplified model, only the material properties of the gray matter are used because the primary interest region (the surface of the brain) consists of gray matter only. The dura and the pia/arachnoid were both defined as elastic material. All the material properties are listed in Table 2.1. The skull and indenter were assigned to be rigid.

2.1.4 Mesh Convergence

Mesh is important in FE analysis, and results can vary based upon the mesh. A coarse mesh with large elements might produce less accurate results. A dense mesh provides more accurate results, but also lengthens computation time. A mesh convergence study seeks to find the coarsest mesh that will still give an accurate result, thus minimizing computation time. Six different element sizes (varying from 97 to 147 μm in 10 μm increments) were used to investigate convergence. Three elements on the surface of the

brain (one element at the center of the indentation and two around the boundary of the craniotomy) were picked to compare the Green-Lagrange first principal strain. Maximum strains at the three regions for each element size were plotted on Figure 2.2. As shown in Figure 2.2, element sizes from 97 to 117 μm yielded constant results. When the brain was meshed with the 117 μm solid elements, it consisted of 429,318 elements. As long as the brain was meshed with the size smaller than 117 μm and had more than 429,318 elements, the model produced consistent results. Based on this analysis, the final model was composed of a total of 678,363 elements.

2.1.5 Validation Model

Mathur [23] built a FE validation model for quantifying deformations during CCI. Predictions from Hertz contact theory were compared to the results of the validation model. A simple rigid indenter and a rectangular block, which was assigned the elastic material properties, were built. The same material properties and contact algorithm were used for this research and Mathur's model; therefore, the validation model would be identical. The validation model is not included in this thesis. Mathur reported normal and shear stresses from the FE model to compare with those from Hertz theory. The difference was less than 5%, and the maximum stresses were located at the subsurface. That teaches us that the model was validated since the model results are in agreement with the Hertz theory results.

2.2 Influence of Ventricles

One of the main functions of cerebrospinal fluid (CSF) in the ventricles and the subarachnoid space is to protect the brain from injury. In the Mathur model [23], there are no ventricles in the brain, but only brain tissues. Considering the protection function of

the ventricles and meninges, we sought to investigate the influence of the ventricles on cortical deformations. The ventricles were digitized from the same images of the C57BL/6J male mouse brain that was used to create the rest of the brain.

2.2.1 Ventricles

The brain contains four fluid-filled ventricles: two lateral ventricles, the third ventricle and the fourth ventricle. A lateral ventricle curves through each cerebral hemisphere. The lateral ventricles are the largest ventricles of the brain and follow C-shaped courses. Most of the cerebrospinal fluid (CSF) is produced in the lateral ventricles, and they contain almost all of the ventricular CSF. The third ventricle is connected to the lateral ventricles by interventricular foramen. The fourth ventricle is connected to the third ventricle by the cerebral aqueduct and also to the central canal of the spinal cord. The fourth ventricle has additional passages to the subarachnoid space. Therefore, CSF is allowed to flow into the subarachnoid space. [18]

The ventricles are filled with CSF, which has three main functions [18]. First, CSF protects the brain from trauma. It acts as a cushion to protect the brain from direct application of force. Second, it eliminates wastes from nervous tissues and also provides nutrition to them. Third, CSF in the subarachnoid space supports the brain due to a buoyancy effect. This buoyancy effect helps decrease the weight of the brain, reducing the pressure to the bottom of the brain [18].

2.2.2 Simplification of the Ventricles

Generating hexahedral elements is time consuming. As the surface defining the ventricles becomes more complex, more time is needed to create mesh. The geometry of the ventricles was simplified to create well-organized hexahedral elements for both the brain and the ventricles. The indenter was located at a distance of 0.2 mm posterior of the bregma and 3 mm lateral of the sagittal suture. Figure 2.3 shows that only one ventricle is in close proximity to the indenter.

If the ventricle closest to the indenter (purple element), which is filled with CSF, does not have any influence on the cortical strain compared to the model without ventricles, it provides reason to ignore the ventricles when building a CCI model. Because of the symmetry, only the ventricle closest to the indenter (lateral ventricle) remains, and there is another ventricle on the other hemisphere to consider (Figure 2.4).

2.2.3 Contact

The contact between the ventricles and the brain was defined with “LAGRANGE_IN_SOLID”. “LAGRANGE_IN_SOLID” defines interactions between fluid (Arbitrary Lagrangian-Eulerian (ALE)) and solids (Lagrangian) modeled with separate meshes. Coupling between solid and fluid (ALE) and leakage control of fluid were adjusted using the “LAGRANGE_IN_SOLID” card. When this card is used, a void part is required to support the flow of fluid in the model. The void part allows the motion of CSF within the void parts under the deformation of the brain tissue. The fluid parts share nodes with each other, but not with the solid parts. In other words, the void part and the ventricles share nodes at the boundaries, but the brain does not share nodes with the void and the ventricles. The elements of the void and the brain overlap, but there is no

interaction between them, and the void only exists to allow the motion of CSF inside the ventricles. HOURGLASS was used to reduce zero energy modes, which produce zigzag deformation of elements, and to stabilize the brain under the impact [23].

2.2.4 Significance of the Ventricles

Three different models were used to investigate the influence of the ventricles. To focus on the qualitative properties, the model must be simplified to reduce computational time. Also, if the main interest of the model is at the surface of the brain, the ventricles might not be a significant factor on the exterior. The model with the ventricles has the same setup as the baseline model with the exception of CSF inside the brain.

The scanned images of C57BL/6J male mouse used to build the FE model in this research do not represent all mice brains because the shape and location of the ventricles vary in the real world. A model with bigger ventricles can elucidate the influence of the ventricles in the simplified CCI model to account for the variation in ventricle size. Another model has 1.5 times larger diameter of the lateral ventricles than the previous ventricles and is closer to the surface of the brain (Figure 2.4). All other setups are the same. As shown in Figure 2.5, three points were chosen from the surface to the deep to observe the variation of strain depending on the depth.

In Figure 2.6, point A was the closest to the surface of the brain, and point C was the farthest from the surface but closest to the ventricles, and point B was in between point A and C. The difference in the maximum principal strain of point C (Figure 2.6(c)) between the model without ventricles and the model with bigger ventricles was about 10%. However, the same evaluation in point A (Figure 2.6(a)) had a difference of about 3 percent. The brain elements near to the ventricles were influenced, but not the elements

on the surface. In regards to the fact that the main area of interest in this research is the study of the brain surface and the difficulty of generating the interior geometries of the mesh models, we reason that it is not necessary to include the ventricles in this model. If, however, a study aims to obtain accurate results on the interior of the brain, ventricles should be included. The ventricles were not included for any results in Chapter 3.

2.3 Element Types

As already noted, generating a reliable mesh is important in FEM. A high quality mesh with sufficient refinement is critical to accurate results. As the geometry of the model becomes more complex, intensive labor is required to generate the mesh. The geometry of the ventricles is complex, making the inner surface of the brain surrounding them also complex. In general, hexahedral elements are more widely used over tetrahedral elements due to the accuracy of the results [20]. Tetrahedral elements are known to have a tendency for volumetric locking [21]. Locking means that FE models exhibit a stiff response under deformation, especially in nearly incompressible materials, plasticity, and acute bending. Hexahedral conformations do not have the locking issue [22]. However, tetrahedral elements are simple to use for complicated geometries. Meshing complex geometries with hexahedral elements, on the other hand, is time consuming, and achieving a high quality representation is difficult.

LS-DYNA provides advanced tetrahedral element formulations. ELFORM=16 is the 2nd order tetrahedral element also known as 10-node-tetrahedral, which has good accuracy for moderate strains. ELFORM=13 has formulations for one point constant stress with nodal pressure averaged. ELFORM=13 can alleviate volumetric locking. Both ELFORM=13 and 16 have better performances than the linear tetrahedral elements and

reduce volumetric locking. However, ELFORM=16 is not suited for large strains, and ELFORM=13 needs a finer mesh and has a limited use, as not all the material types support it. Advanced tetrahedral element types are not suited for brain modeling because CCI is a large deformation model, and the brain requires a material model that ELFORM=13 does not support. Table 2.2 shows a comparison of element types.

Biological models normally have complex geometries that are challenging to model with hexahedral elements. In the model of the brain, its inner surfaces are complex due to the geometry of the ventricles. The brain model was divided into small components to generate the mesh, and the model is mostly constituted of hexahedral elements with some linear tetrahedral elements. The mixture of hexahedral and tetrahedral helps to construct mesh for the ventricles in the brain, but verification is required for the results to be reliable.

A simple verification has been made to examine if the tetrahedral elements have any influence on the model such as volumetric locking. Three different models were generated to investigate the influence of meshing. The brain models had ventricle geometries inside, but the ventricles were given brain material properties, rather than those of a fluid. Therefore, the inner geometry of the brain was complex, but all regions were represented as brain tissue.

Figure 2.7(a) contained simplified ventricles (Figure 2.4) and was meshed with 100% hexahedral elements. Figure 2.7(b) incorporated complex ventricles and consisted of 100% tetrahedral elements. Figure 2.7(c) was comprised of complex ventricles and was assembled with 90% hexahedral elements and 10% tetrahedral elements.

Figure 2.8 shows that the region directly under the surface of the brain within the craniotomy where the indenter impacts was of primary interest. Three nodes inside the

brain were selected from the cut section (Figure 2.8), and the Green-Lagrange strains were compared to investigate differences between the models.

A 0.7 mm depth of indentation was simulated during 0.15 ms at 4.7 m/s. After 0.15 ms, the indenter was released. In Figure 2.9, the 100% tetrahedral element model exhibited stiff behavior. As the indenter was released, the strain weakened and started to restore its original geometry, resulting in volumetric locking. The 100% hexahedral elements model and the mixture of hexahedral and tetrahedral elements model had almost identical results. In these cases, strains continued to increase after maximum indentation due to the inertia of the brain tissue. There were no sudden changes of strain at any point, and the curves were smooth. This is because there were no tetrahedral elements under the indenter in the mixed elements model. Using different element types in regions other than directly under the indenter does not have a significant influence on the results. However, when the ventricles are filled with CSF, not solid material, and the ALE card is used for CSF and the void part, tetrahedral elements do not support the ALE card. ALE works only with hexahedral elements. Therefore, the model geometry needs to be simplified in order to use 100% hexahedral elements.

2.4 Transformation of Strains

Figure 2.10 shows that there was a larger deformation on the surface compared with the deformation of elements in the deep brain. Due to the large deformation, strains in the local and the global coordinate systems are significantly different. Local coordinate systems aligned with the brain surface allow analysis of strains that are relevant to pial blood vessels running along the brain surface. LS-Dyna provides the strain in the local coordinate system only for shell elements, not for solid elements; therefore, manual

conversion was needed to plot the strains on the surface of the brain in the local coordinate system using Matlab.

2.4.1 Method of Transformation

Figure 2.11(a) shows a random selection of deformed elements on the brain surface from the top view. Local x and z vectors for each element, shown as $x1$ and $z1$, were defined using the nodal coordinates of each element and are thus generally not perpendicular to each other. For each element, a vector normal to the $x1$ - $z1$ plane was calculated as the cross product of $x1$ and $z1$, represented by $n1$ shown in Figure 2.11(b). The $z2$ vector, which is on the $x1$ - $z1$ plane and perpendicular to the $x1$ vector, was defined as the result of the cross product of $n1$ and $x1$.

All local coordinate systems had different orientations, leading to difficulty in relating surface strains from neighboring elements. In order to maintain consistency, a local $x1_p$ axis was defined as being the same as the projected global X axis on the $x1$ - $z2$ plane of each element as shown in Figure 2.12(a). Local $x1_p$ axes were aligned with the global X axis and rotated about the $z2_p$ axis due to the deformation by the indenter.

$x1_p$ and $z2_p$ vectors were calculated using Equations 2.2 and 2.3.

$$x1_p = \frac{X - (X \cdot n1) n1}{|X - (X \cdot n1) n1|} \quad (2.2)$$

$$z2_p = \frac{Z - (Z \cdot n1) n1}{|Z - (Z \cdot n1) n1|} \quad (2.3)$$

Z is the global Z axis. And the rotation matrix is,

$$R = \begin{bmatrix} X \cdot x1_p & X \cdot n1 & X \cdot z2_p \\ Y \cdot x1_p & Y \cdot n1 & Y \cdot z2_p \\ Z \cdot x1_p & Z \cdot n1 & Z \cdot z2_p \end{bmatrix} \quad (2.4)$$

Y is the global Y axis. Local strain tensor is calculated by

$$e = R^T E R \quad (2.5)$$

e is the Green-Lagrange strain tensor in local coordinate system

E is the Green-Lagrange strain tensor in global coordinate system exported from LS-Dyna

R is the rotation matrix.

Green-Lagrange strain tensors in the global coordinate system were exported manually by selecting elements on the brain surface. Matlab code is included in the Appendix.

2.4.2 Single Element Test

The first principal strain in the local coordinate system was calculated by solving the eigenvalue problem for the local strain tensor. The equations above were verified with a single element tensile test. As shown in Figure 2.13(a) and (b), a single hexahedral element was rotated -30° about the Z axis. The element was then stretched 200% in the local x direction. The associated Green strain for the local stretch equation is calculated as

$$e_G = \frac{1}{2} (\lambda^2 - 1) \quad (2.6)$$

where λ is the stretch ratio.

Therefore, the Green strain in the local x direction was 1.5. The strain calculated using Equation 2.2 to Equation 2.6 in Matlab was 1.4966. Thus, the equations and the associated Matlab code worked in this 2D rotation. A 3D test was also performed as shown in Figure 2.13(c) and (d). The element in 3D space was rotated -30° about both the

Y and Z axes and then stretched 200% in the local x direction. The Green strain in the local x direction calculated by Equation 2.6 was 1.5. The strain calculated using Equation 2.2 to Equation 2.5 in Matlab was 1.4451. The difference is 5.5%, and it can be concluded that the equations and the Matlab code worked in 3D as well.

2.4.3 Cube Test

The brain model has complex geometry and consists of many parts that have different material properties and constitutive models. Strains need be converted manually into the local coordinate system. Because of this complexity and coordinate system conversion, predicting results for the model is not straightforward, making it difficult to determine if postprocess results are correct. It was deemed necessary to build a simple model, the results of which were used to give confidence to the predictions. In this model, the solid cube represents the brain, and it is surrounded by shell elements which represents PAC. The indenter was built right above the PAC (Figure 2.14). The indenter is identical to the indenter in the realistic brain model in terms of geometry, and it penetrates the cube to the same depth (0.7 mm) and with the same velocity (4.7 m/s) as in the baseline brain model. All the material properties are the same as those of the brain model.

Green-Lagrange strain distributions in the local coordinate system on the surface of the cube model at the maximum indentation (0.7 mm) are shown in Figure 2.15. The diameter of the plot is approximately 3.3 mm, which is slightly bigger than the diameter of the indenter. The maximum strain appears at the center of the indentation. In Figure 2.15(a), the first principal strain distribution has a circular pattern, centered at the middle of the craniotomy, and the magnitude of the strain decreased as the distance from the center increased. Figure 2.15(b) and Figure 2.15(c) show the strains in radial and

circumferential directions, respectively. The circumferential strain is a primary contributor to principal strain over the whole craniotomy, while the radial strain is high in the center, yet contributes little to tensile strains away from the very center.

Three Green-Lagrange strains on the surface of the brain were reported in the results section in Chapter 3: first principal strain, radial strain, and circumferential strain.

2.5 Parameter Study

Five different parameter studies were performed in order to investigate the relationships between the different brain tissue responses and each parameter. The baseline model has the craniotomy on the skull about the same size as the diameter of the indenter, and the depth of the indentation was 0.7 mm. The tip shape of the indenter is hemispherical. The indenter was located at a distance of 0.2 mm posterior of the bregma and 3 mm lateral of the sagittal suture. In the experiment, the angle of the indenter is adjusted until it appears to the experimenter to be perpendicular to the surface of the brain. In the base FE model, the indenter is rotated by 30° because this is perpendicular to the brain surface. The conditions in the baseline FE model were designed to match those of the experiment.

2.5.1 Loading Conditions

Different loadings produce different strain distributions on the surface. 4.7 m/s is the baseline indenter velocity for CCI experiment in our lab. Two different velocities of the indentation and two different depths of the indentation were performed. They are listed in Table 2.3.

2.5.2 Craniotomy Size

The brain consists of nearly incompressible material. When the brain is compressed by the indenter, there is not enough space to move; therefore, the brain would come out of the skull (Figure 2.16). There will be high strains on the portion of the brain jammed between the skull and the indenter. If the size of the craniotomy is increased, the results will be changed. The craniotomy size of the baseline model was 3.2 mm, and the large craniotomy size was 4.4 mm. The craniotomy size is 1.375 times bigger than the baseline model.

2.5.3 Indenter Angle

The indenter is rotated by 30° to be perpendicular to the surface of the brain. Even though the surface of the brain is not flat, the indenter mostly presses the brain evenly. This study focused on characterizing the change of the strain distribution on the surface of the brain with a different indenting angle. The indenter is tilted 15° relative to the surface of the brain as shown in Figure 2.17.

2.5.4 Indenter Tip Shape

Different tip shapes produce different strain concentrations, especially if there are edges on the tip. The tip was hemispherical in the base model, and a flat tip indenter was built to observe how changing the shape of the tip would influence the strain field on the surface of the brain (Figure 2.18). The indenters were both given the same diameter (3.05 mm). Other parameters were set the same as the baseline model.

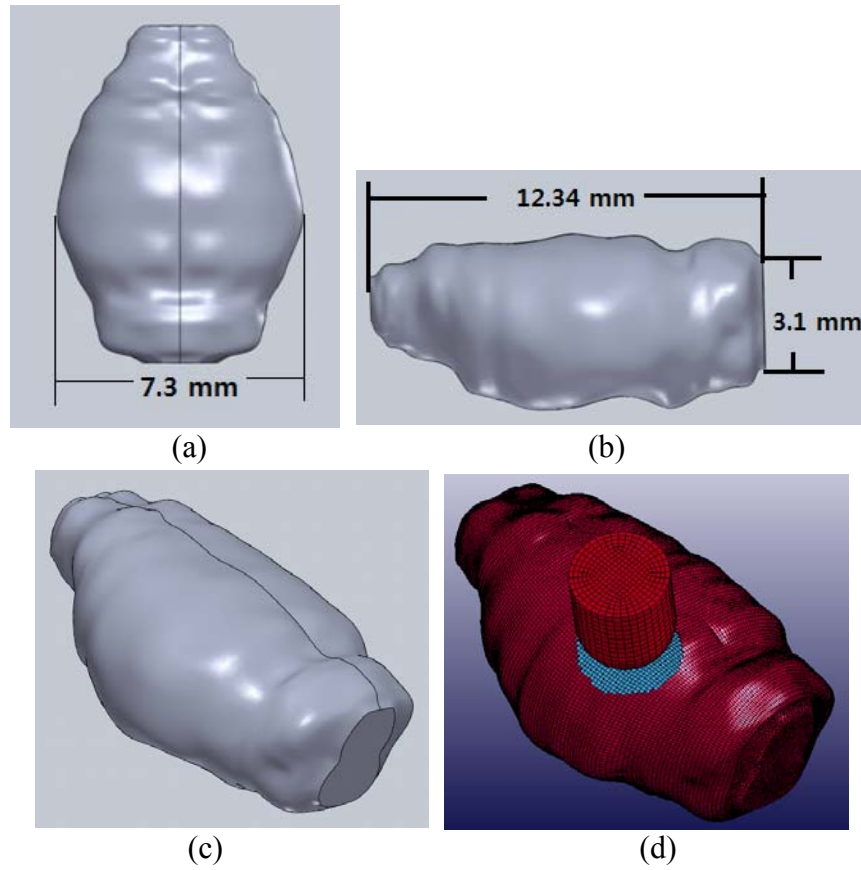


Figure 2.1. 3D mouse brain model in (a) Top, (b) left, (c) isometric views, and (d) isometric view of CCI model.

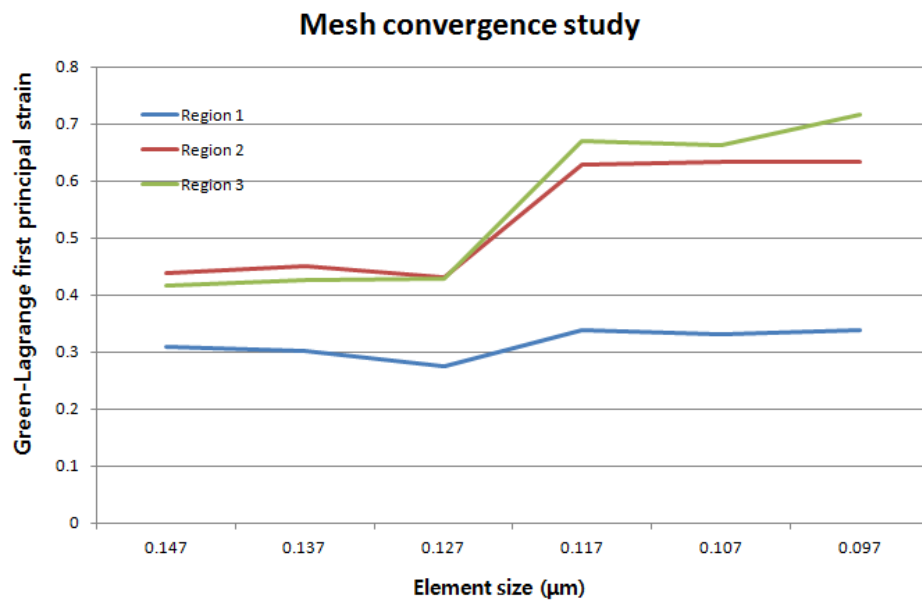


Figure 2.2. Results of mesh convergence study.

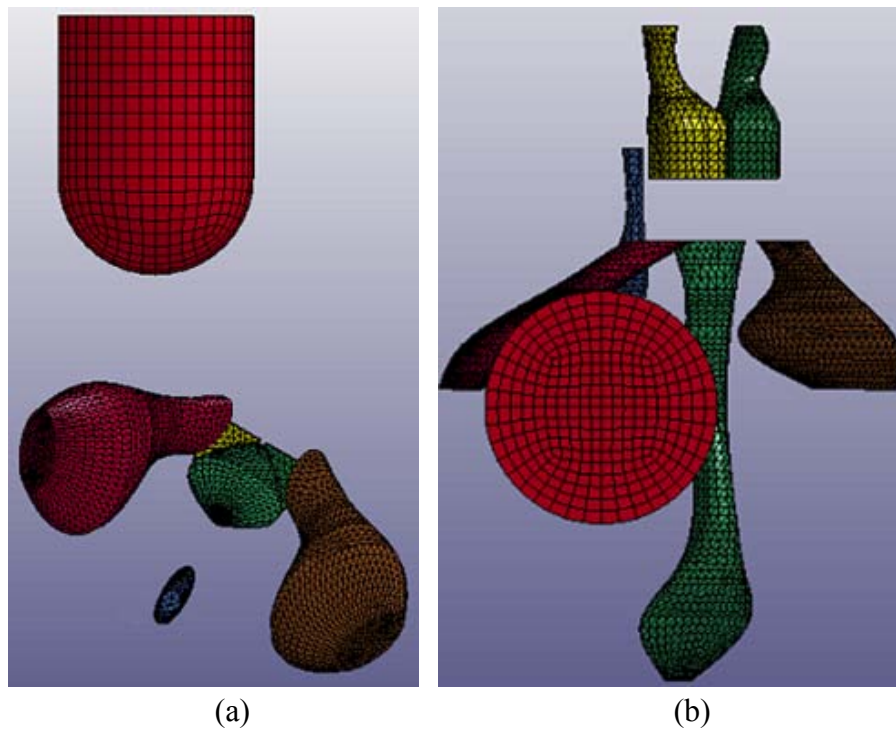


Figure 2.3. 3D mouse ventricles and indenter. (a) Front, and (b) top views.

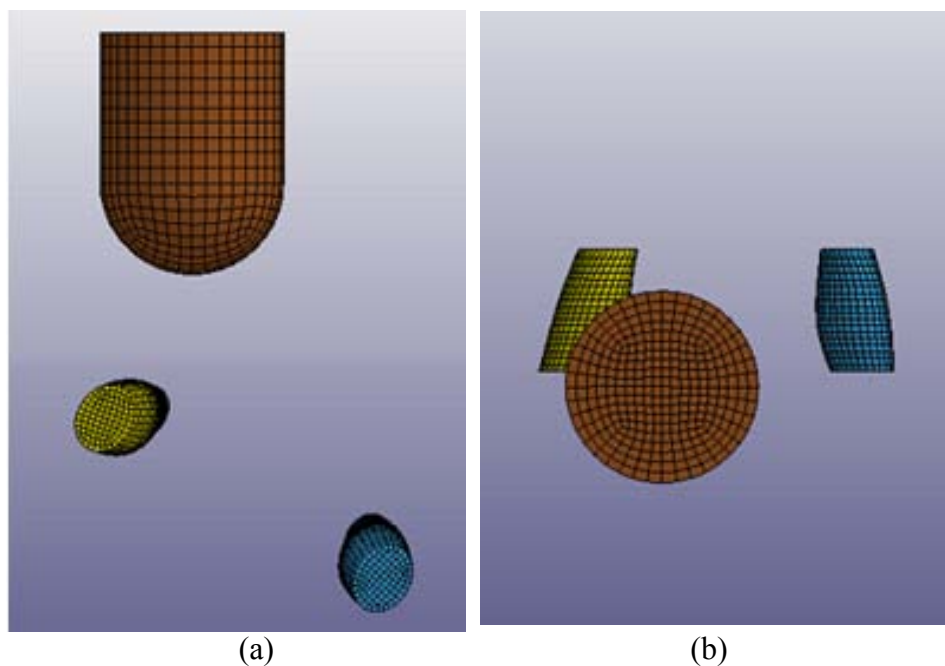


Figure 2.4. 3D model of ventricles and indenter. (a) Front, (b) top views of simplified ventricles and indenter, and (c) front view, (d) top views of simplified big ventricles and indenter

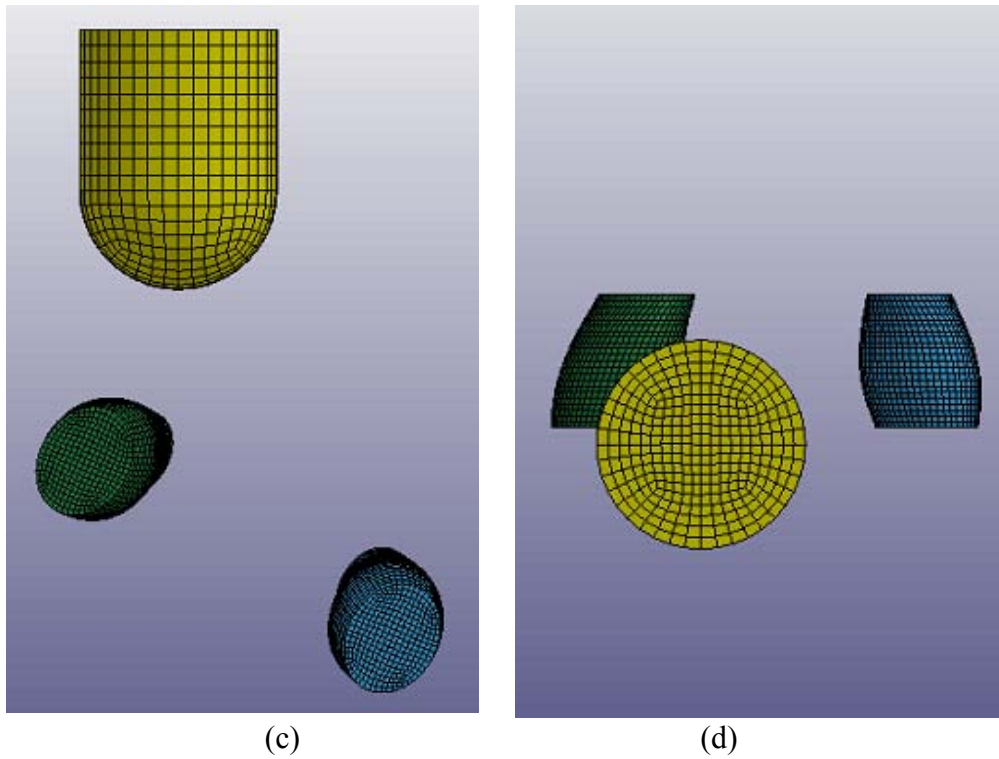


Figure 2.4 continued.

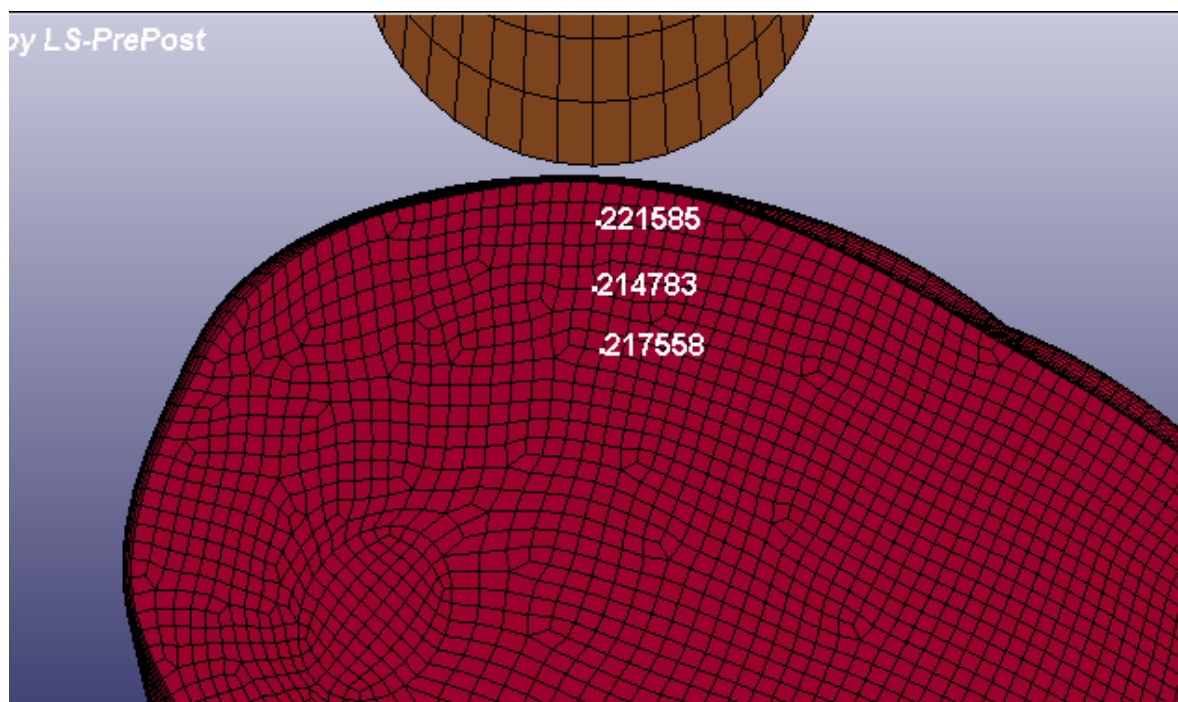
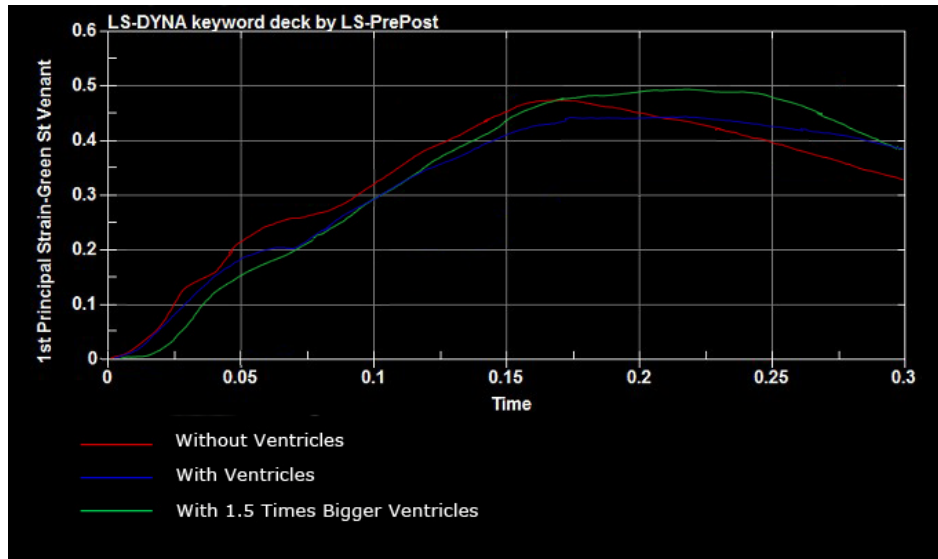
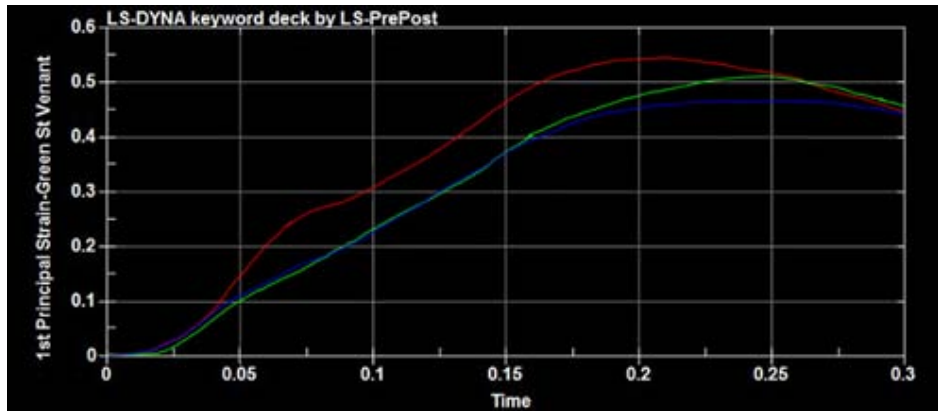


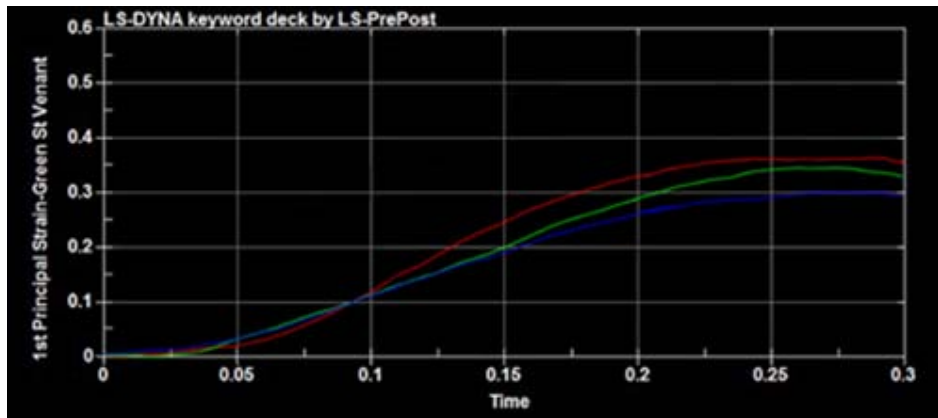
Figure 2.5. Three nodes were picked to observe strain in each model.



(a)



(b)



(c)

Figure 2.6. Green-Lagrange first principal strain of (a) point A, (b) point B, (c) point C.

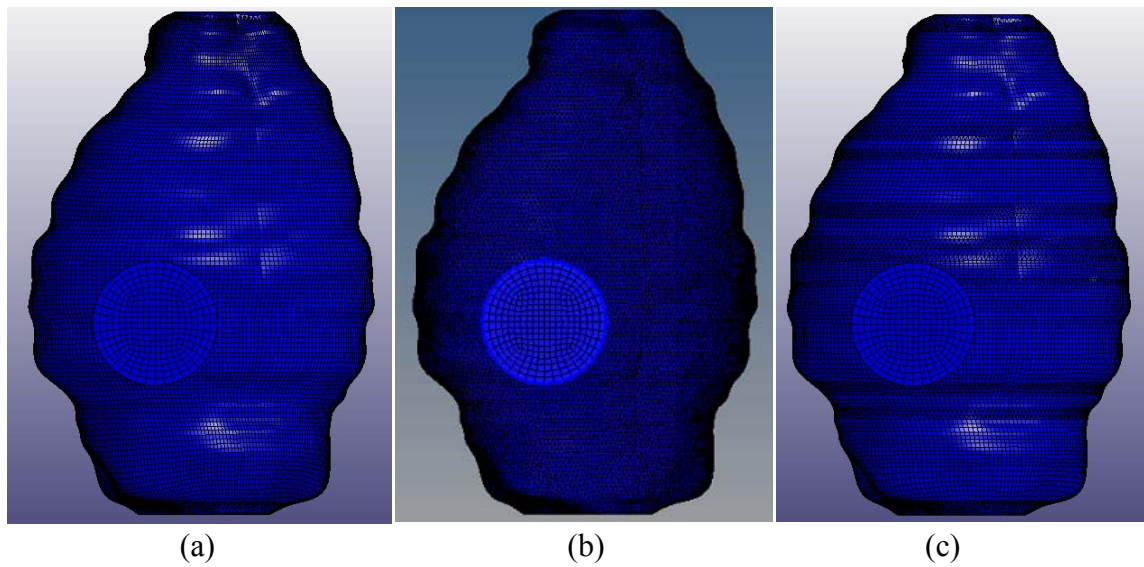


Figure 2.7. Top view of the brain model with (a) 100 % hexahedral elements, (b) 100 % tetrahedral elements, and (c) a mixture of hexahedral and tetrahedral elements.

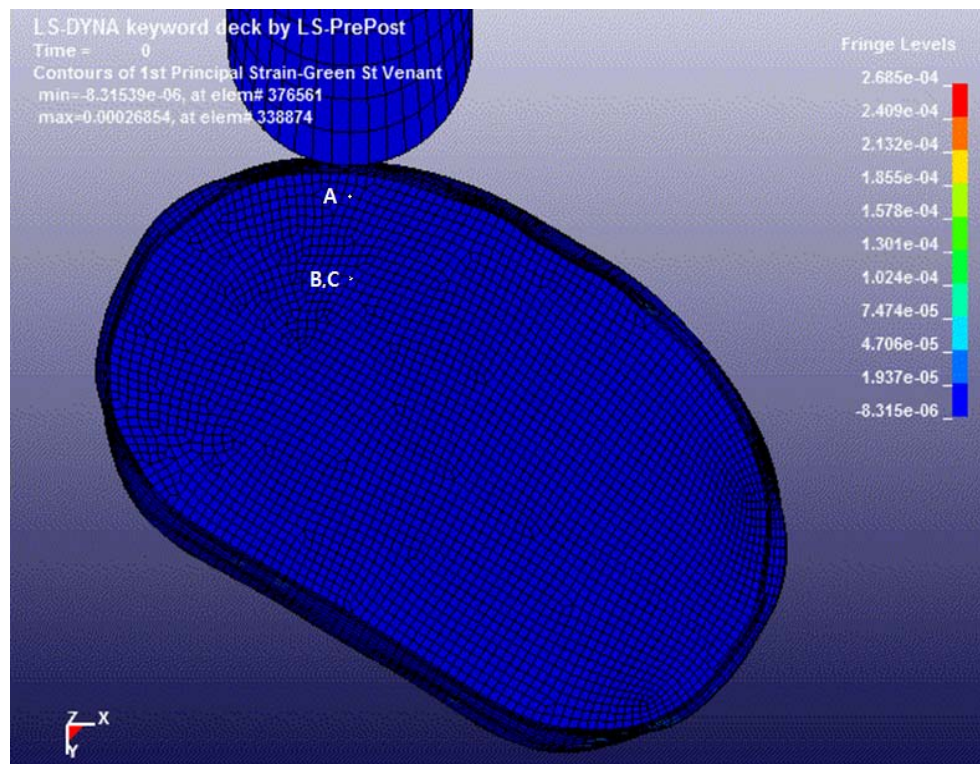
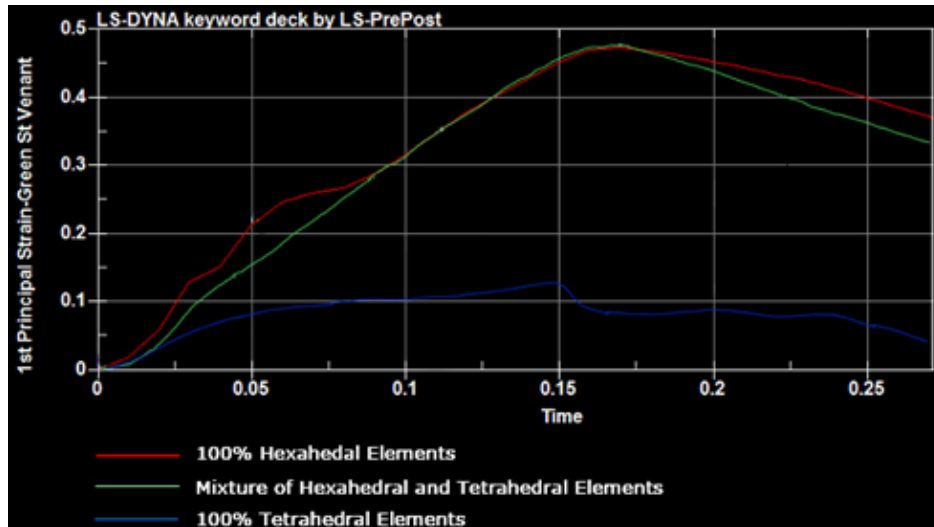
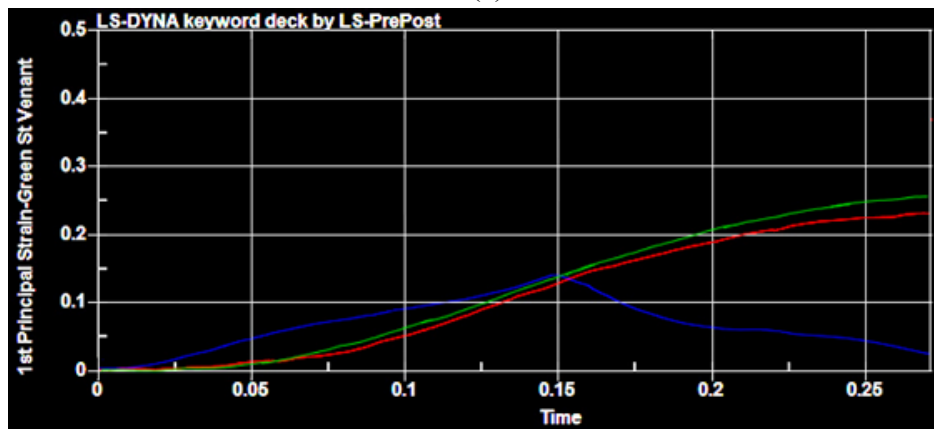


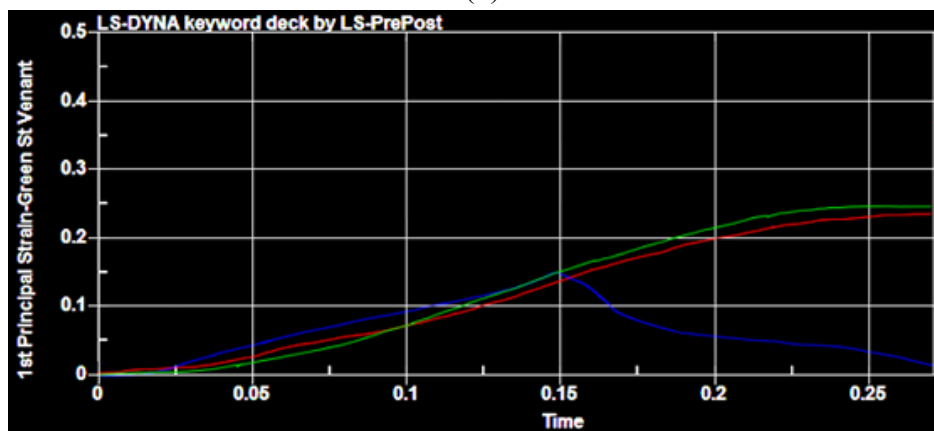
Figure 2.8. Three nodes were picked to observe strain in each model. C was positioned laterally 250 microns from B.



(a)



(b)



(c)

Figure 2.9. Green-Lagrange first principal strain of (a) point A, (b) point B, and (c) point C.

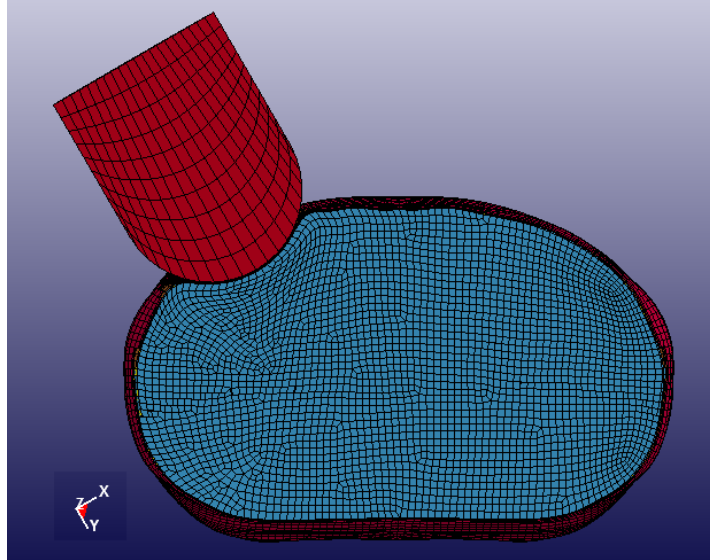
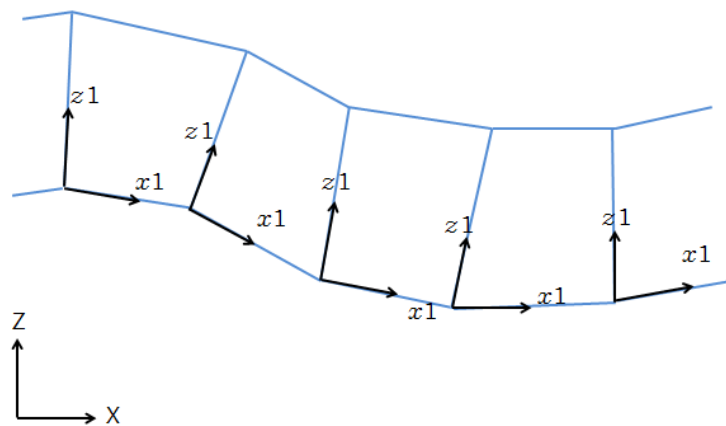
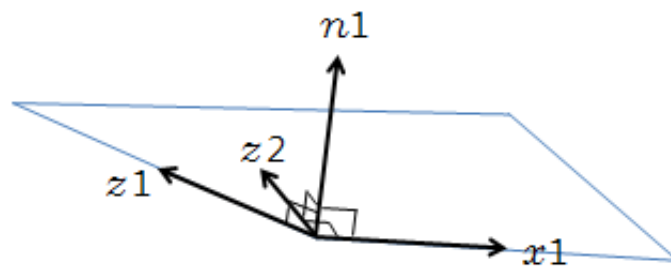


Figure 2.10. Deformation on a coronal section of the brain tissue at the center of the impact site at maximum indentation.



(a)



(b)

Figure 2.11. Local coordinate system defined for deformed elements in (a) top and (b) isometric views.

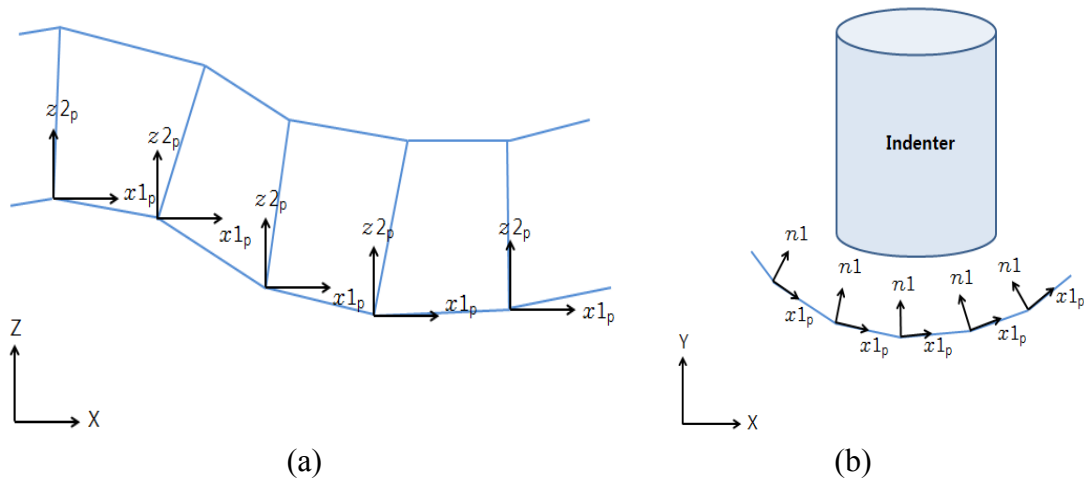


Figure 2.12. Revised local coordinate system of each deformed element.
 (a) Top, and (b) cut views.

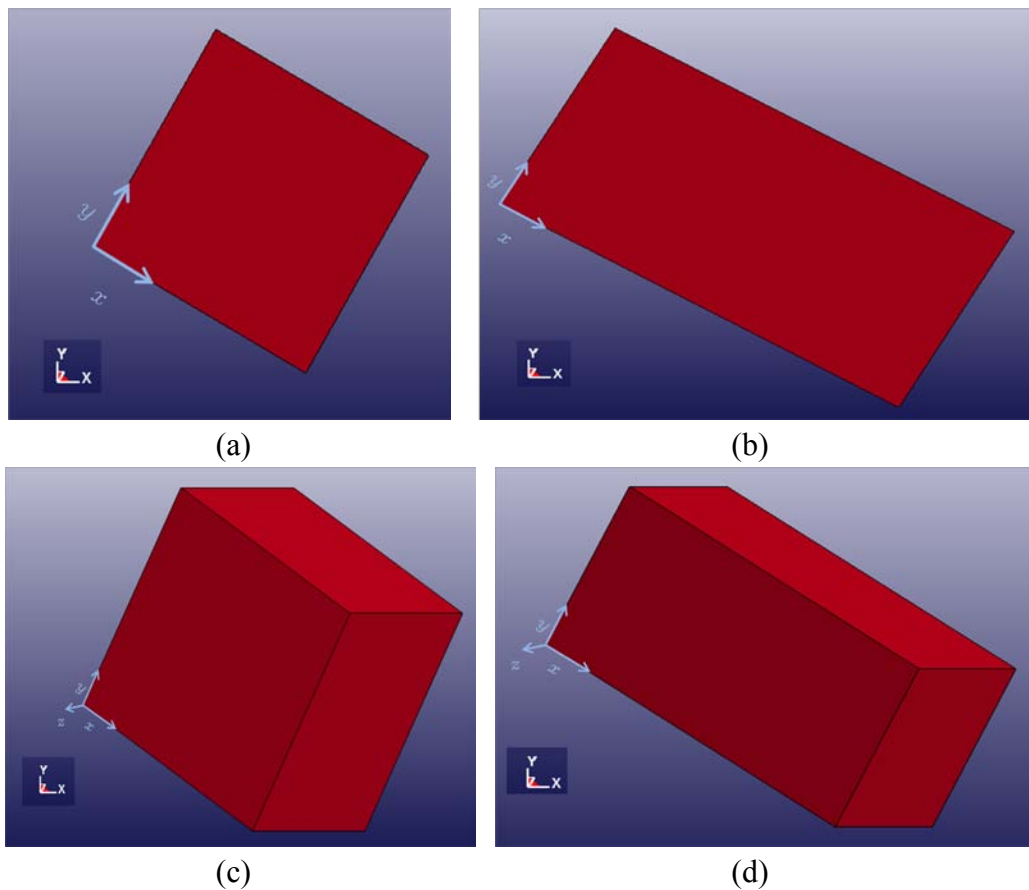


Figure 2.13. Verification model in 2D (a) before, (b) after it was stretched, and in 3D (c) before, (d) after it was stretched.

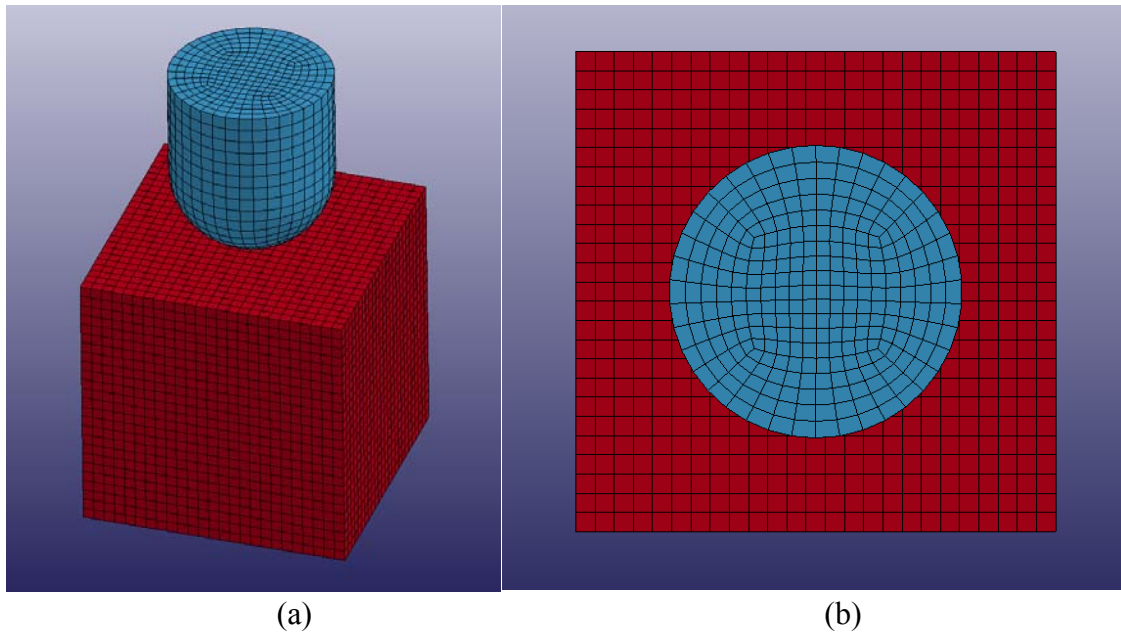


Figure 2.14. Verification model. (a) Isometric, (b) top views of the model consisted of the brain, PAC, and the indenter.

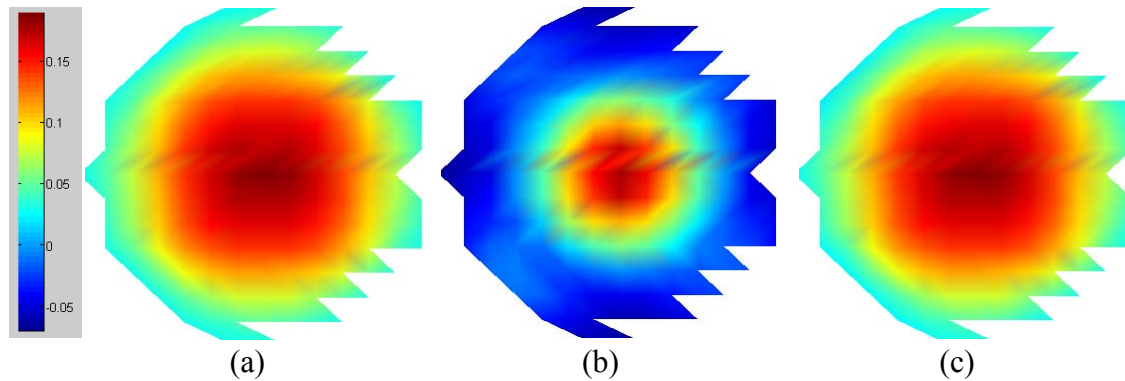


Figure 2.15. Green-Lagrange (a) first principal strain, (b) radial strain, and (c) circumferential strain on the surface of the verification model relative to the geometry of the indenter.

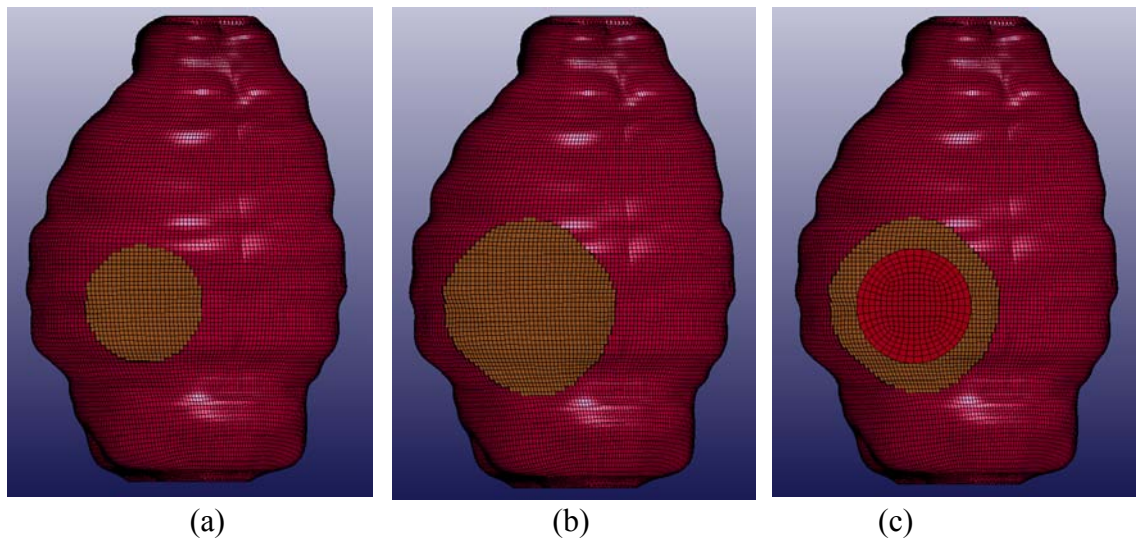


Figure 2.16. Different craniotomy size: (a) baseline model, (b) large craniotomy model, (c) large craniotomy model with indenter.

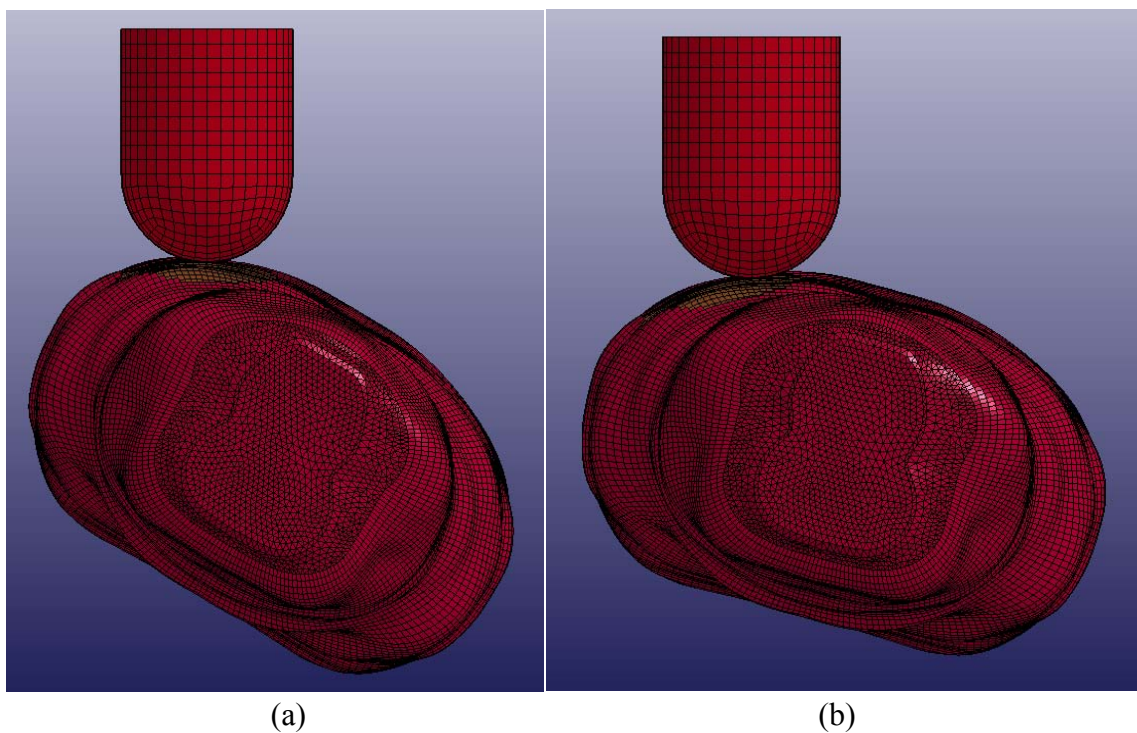


Figure 2.17. Different indentation angle: (a) Baseline model, (b) 15° tilted model.

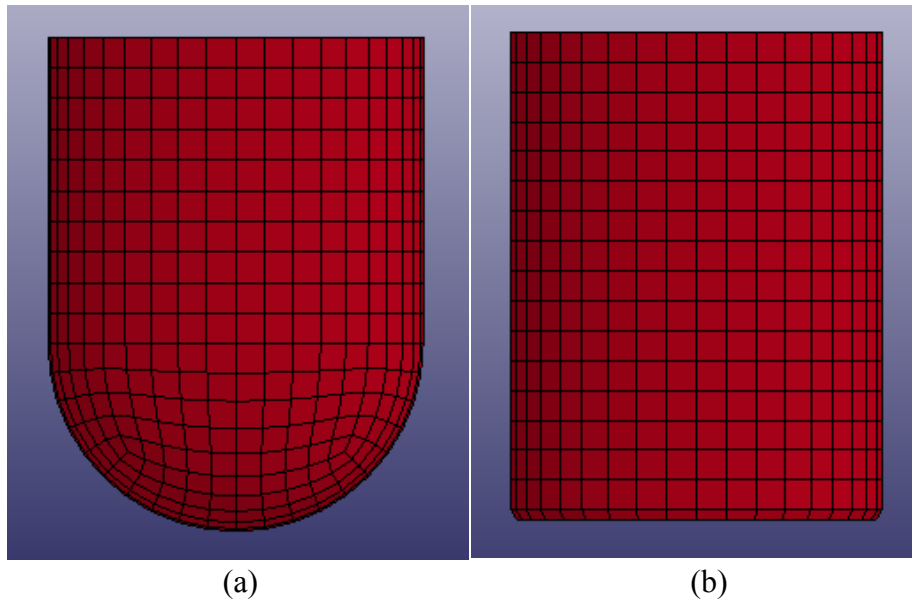


Figure 2.18. Indenter tip shape: (a) Baseline indenter, (b) flat tip indenter.

Table 2.1. Material properties of the mouse brain and the meninges [7]

Mouse Brain	Density	1040 Kg/m ³
	Bulk Modulus	2.1 GPa
	Long Term Shear Modulus	0.51 kPa
	Short Term Shear Modulus	1.72 kPa
	Decay Constant	20 ms
Dura	Density	1040 Kg/m ³
	Elastic Modulus	31.5 MPa
	Poissons Ratio	0.45
PAC	Density	1130 Kg/m ³
	Elastic Modulus	12.5 MPa
	Poissons Ratio	0.45

Table 2.2. Different element types [24]

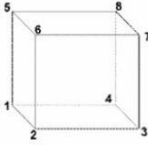
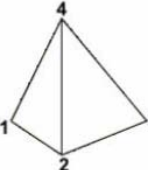
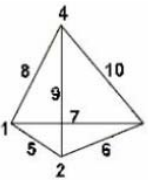

Element type	Shape	Result accuracy	Mesh	Computational time
8-noded hexahedral		Good	difficult	Long
4-noded tetrahedral		Poor	Easy	Short
10-noded tetrahedral		Good	Easy	Long
4-noded tetrahedral with averaging nodal pressure		Good	Easy	Fair

Table 2.3. Loading condition study

	Indenter Velocity (m/s)	Indentation depth (mm)
Baseline	4.7	0.7
High rate	7.05	0.7
Low rate	2.35	0.7
Deep depth	4.7	1.05
Shallow depth	4.7	0.35

CHAPTER 3

RESULTS

All results of the mouse brain model are included in this section. Green-Lagrange strain distributions on the surface of the mouse brain are reported. The area of interest was the surface of the brain within the craniotomy since there were not many variations on the outside of the craniotomy (under the skull). The strain was plotted in the local coordinate system at the moment of the maximum indentation.

3.1 Base Model

Figure 3.1 shows the cut view of the brain model, and the maximum principal strain appeared at subsurface location. Figure 3.2(a), (b), and (c) represent the Green-Lagrange strain distribution on the surface of the mouse brain for the base line model, and Figure 3.2(d) plots corresponding strain values along the diameter of the craniotomy. The baseline model had an indentation depth of 7 mm at 4.7 m/s. Figure 3.2(a) shows that the maximum first principal strain occurred at the center of the indentation, with a magnitude of 0.2507 strain. The first principal strain distribution has a circular pattern, centered at the middle of the craniotomy, and the magnitude of the principal strain decreased as the distance from the center increased. Figure 3.2(b) and (c) show the strains in the radial and circumferential directions, respectively. Circumferential strain is the primary contributor to principal strain over the whole craniotomy, while radial strain is high in the center but

contributes little to tensile strains away from the very center. The elements at the center of the indentation experienced the highest tensile strains in the radial and circumferential directions. Some elements were compressed in the radial direction, while the tensile strains occurred in the circumferential direction. Figure 3.2(d) shows that elements at the center, where the indenter made direct contact, experienced tension radially, and the rest of the elements experienced compression. The brain tissue right under the indenter had tensile strains in both the radial and circumferential directions with a similar magnitude of strain. However, the area where the indenter did not contact directly within the craniotomy was compressed in the radial direction. This observation is consistent with the idea that the brain tissue under the indenter was pushed laterally during the indentation and pressed into the surrounding brain tissue. Therefore, compression occurred around the indenter in the radial direction. The right side of Figure 3.2(a) and (b) show that radial tension was also produced at the boundary of the craniotomy. In the global coordinate system, compression occurred at this boundary, but the same elements were in tension in the local system. Large distortion on the elements on the brain surface at the right side of the craniotomy boundary produced tension in the local coordinate system. The first principal strain contours did not exactly correspond with the circular craniotomy in the radial direction because the mouse brain was not axisymmetric like the verification model and the brain surface was not a smooth curve.

Figure 3.3 shows the Green-Lagrange first principal strain over the surface as a function of time. Maximum indentation occurred at 0.15 ms, and 0.0375 ms, 0.075 ms, and 0.1125 ms were plotted on Figure 3.3(a) to Figure 3.3(d), respectively. When the indenter started to contact the brain, tensile strain first occurred at the center and

propagated to the boundary of the craniotomy.

3.2 Influence of Indentation Rate

Figure 3.4 shows the cut view of the brain model with different indentation rate, and the maximum principal strain appeared at subsurface location. Figure 3.5(a), (b), and (c) represent the results of the low rate model, and Figure 3.5(e), (f), and (g) plot the results of the high rate model. Figure 3.5(d) and (h) show corresponding strain values along the diameter of the craniotomy. In the low rate model, the indenter struck the brain at 2.35 m/s, which was half the speed of the baseline model. In the high rate model, the indenter moved at 7.05 m/s, which was 1.5 times the velocity of the baseline model. Even though the depth of the indentation was the same as the baseline model, the severity was different in both the low and high rate models. Neither the tensile or compressive strains were as severe as in the low rate model. The overall tensile strain was milder than the baseline model, and the maximum principal strain of the low rate model was 0.1564, which was lower than that of the baseline, which was 0.2507. Figure 3.5(b) shows an asymmetrical strain distribution on the right and left side due to the fact that the brain surface is not evenly rounded.

In the high rate model, the strain at the center of the indentation was about 0.31, which was higher than the baseline model, even though the indentation depth was the same. Interestingly, the maximum first principal strain (0.4882) occurred at the right side of the craniotomy boundary, instead of in the center. Higher magnitudes over the range of the plot were indicated by numbers in the plots. Figure 3.6(a) shows a cross-sectional view of the high rate model at maximum indentation. A zoomed-in view, with the indenter hidden, is shown in Figure 3.6(b). Elements in the boxed region correspond to

the tensile strain area on the right side of Figure 3.6(b). Elements on the surface were pushed aside as the indentation occurred, and due to the inertia and the high rate of the indentation, more distortion was applied on the elements between the indenter and the craniotomy. As a result, the elements experienced tension in the local coordinate system.

3.3 Influence of Indentation Depth

The results of the different indentation depth models are reported in this section. Figure 3.7 shows the cut view of the brain model with different indentation depth, and the maximum principal strain appeared at subsurface location. Figure 3.8(a), (b), and (c) show the results of a small indentation (0.35 mm), and Figure 3.8(e), (f), and (g) represent the results of a large indentation (1.05 mm). Figure 3.8(d) and (h) are corresponding strain values along a diameter of the craniotomy. All other model parameters were the same as the baseline model. Both tensile and compressive strains were milder in the small indentation model. The minimum Green-Lagrange strain was -0.0798, which was significantly lower than -0.2602 of the baseline model. There was not a large compression in the radial direction. Both tensile and compressive strains were milder than the baseline model, and the maximum and minimum strains were 0.1483 and -0.0798, respectively. In the deep depth model, the result was more severe, and tensile and compressive strains were more severe than in the baseline results. Higher magnitudes over the plot range were indicated by the numbers in the plots. Strain at the center of the indentation was higher than in the baseline model, and the maximum first principal strain of 0.4292 occurred at the upper right side of the craniotomy boundary, instead of the center. It can be assumed that this was because the mouse brain was not evenly rounded.

3.4 Influence of the Craniotomy Size

The results of craniotomy size are presented in this section. Figure 3.9 shows the cut view of the brain model with different craniotomy size, and the maximum principal strain appeared at subsurface location. Figure 3.10 shows Green-Lagrange strain distribution. The baseline craniotomy size is about the same as the indenter diameter (3.05 mm), and this model investigated a 30% larger size, which is about 4.4 mm. All other parameters were the same as the baseline model. The maximum strain was 0.2447 at the center and the minimum strain was -0.2652; this was not significantly different from 0.2507 and -0.2602 of the baseline results. One interesting observation is that there was high tension at the boundary of the large craniotomy, similar in magnitude to that at the center of the indentation. Figure 3.11 shows the strain distribution in the global coordinate system, and there was no similarly high tension at the boundary of the craniotomy. Except at the boundary, the strain distributions were similar in the local and global coordinate systems.

Figure 3.12 shows that the whole mouse brain and Figure 3.12(a) had a large craniotomy, and Figure 3.12(b) was the baseline model in the global coordinate system. There was no strain concentration at the boundary of the large craniotomy. Strains in local and global coordinate systems were different, and some elements experienced higher strains in the local coordinate systems than in the global coordinate systems. Therefore, it is important to observe the strain in the local coordinate system to study for vascular injury.

3.5 Influence of Indenter Angle

The effect of using a different indentation angle is shown in this section. In this case, the indenter was tilted 15 degrees from the baseline case; all other parameters were the

same as the baseline model. Figure 3.13 shows the cut view of the model and Green-Lagrange first principal strain in the global coordinate system. The indenter struck the brain from the right side of Figure 3.14(a) to the left with a 15-degree-tilted-angle. As the indenter came from this new angle, the strain concentration appeared opposite to the direction that the indenter came from. The maximum Green-Lagrange strain was 0.4041 located on the left, and the overall strain distribution was biased to the right. Figure 3.15(a) shows a cut view of the brain and the indenter at maximum indentation. Figure 3.15(b) shows the same view magnified with the indenter removed. Elements in the boxed region of interest in Figure 3.15(b) are located where the maximum strain occurred. Most of the elements were compressed between the indenter and the edge of the craniotomy. However, elements on the surface experienced tension by creating a bump on the surface. Only radial strain had high tension on the left and circumferential strain had high tension where the indenter made direct contact. These results demonstrate that both the location and magnitude of the maximum strain can vary by changing the indentation angle.

3.6 Influence of Indenter Tip Shape

The effect of using a different indentation tip shape is shown in this section. Figure 3.16 shows the cut view of indenter tip shape model in the global coordinate system. Figure 3.17(a), (b), and (c) show the effects of a flat tip indenter on the strain distribution. The baseline model used a hemispherical tip, and this model used a flat tip. This variation in tip geometry caused alterations of strain throughout the entire region of interest. The maximum strain did not occur at the center of the indentation because the indenter did not only contact the center, but evenly contacted the brain. However, since the brain surface

is not evenly rounded, the strain was not evenly distributed. The maximum strain of 0.6179 occurred at the boundary of the indenter and was much higher than the strain observed in the baseline model. More brain elements were compressed due to the flat tip, and their motion was limited by the skull; therefore, it resulted in the higher strain. Most of the tensile strain concentration at the edge of the indenter occurred in the radial direction just as in the case where the indenter angle was varied. It can be concluded that the strain distribution on the surface is highly influenced by the shape of the indenter tip.

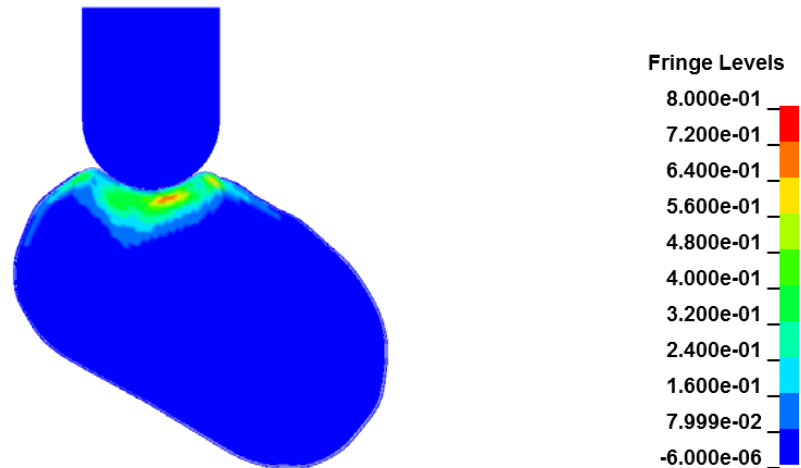


Figure 3.1. Cut view of the brain model with indenter. Green-Lagrange first principal strain in the global coordinate system.

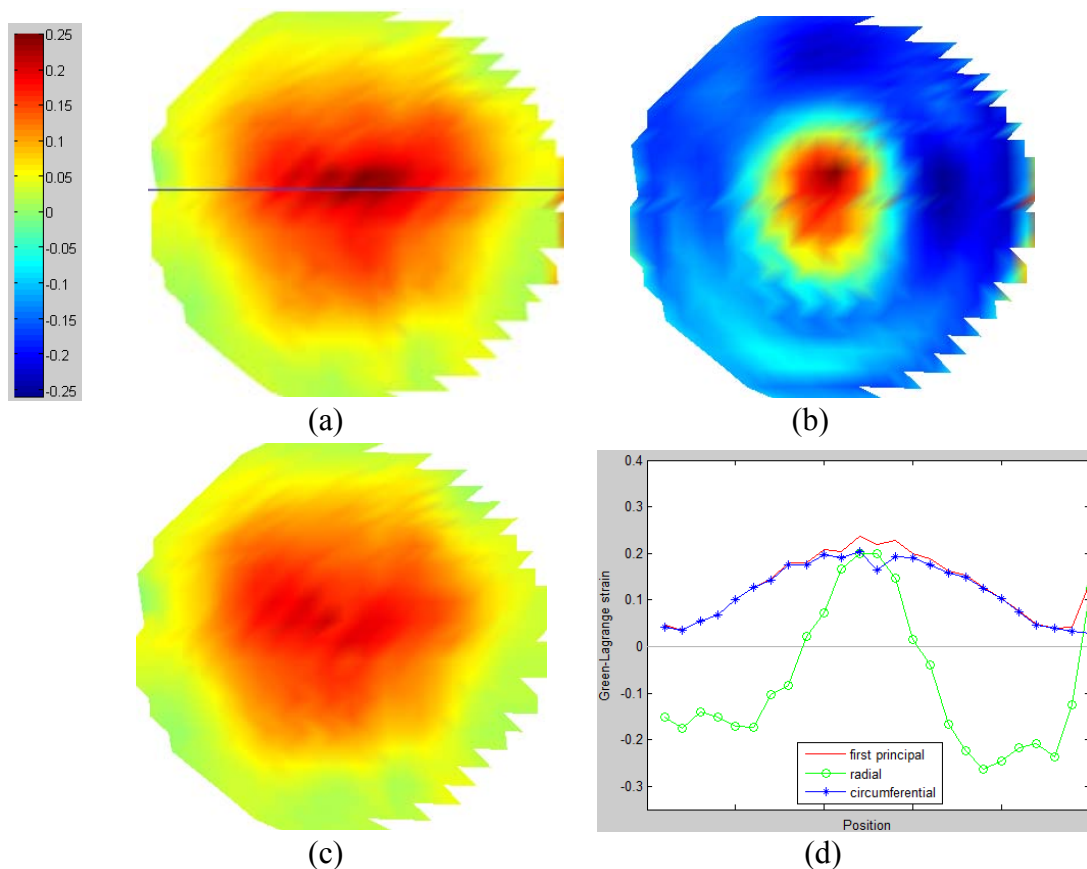


Figure 3.2. Green-Lagrange strain contours and diameter line plots in the local coordinate system on the surface of the brain: (a) first principal strain, (b) radial strain, (c) circumferential strain, and (d) corresponding strain values along the diameter of the craniotomy.

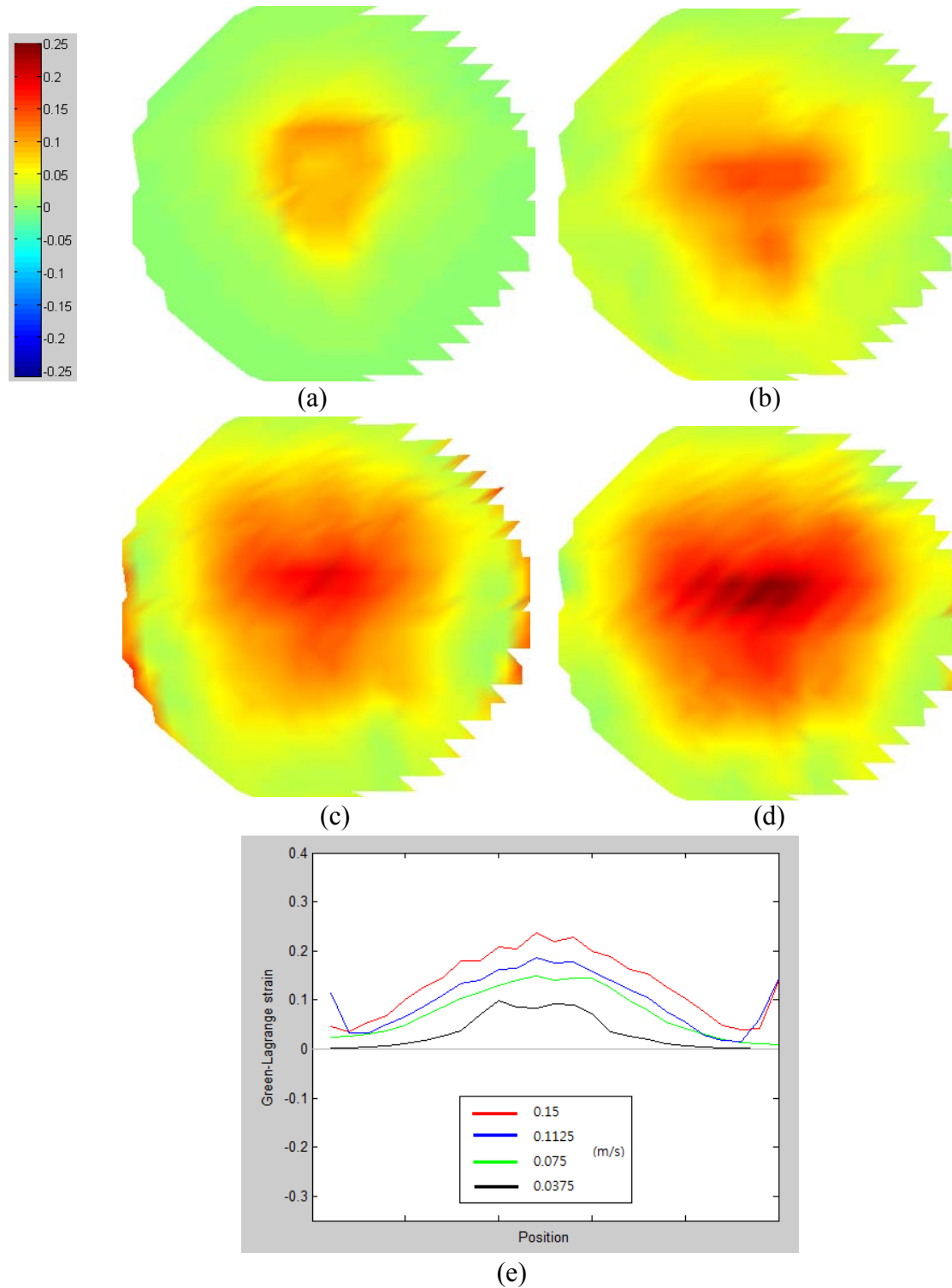


Figure 3.3. Green-Lagrange first principal strain distribution in time frame. (a) 0.0375 ms, (b) 0.075 ms, (c) 0.1125 ms, (d) 0.15 ms (maximum indentation), and (e) corresponding strain values along the diameter of the craniotomy.

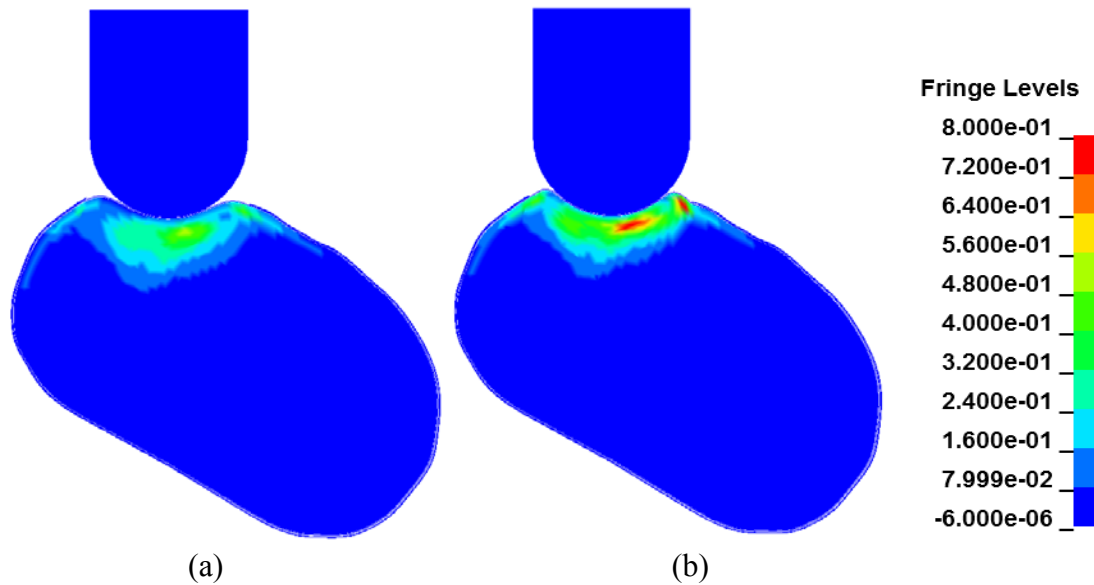


Figure 3.4. Cut view of (a) low rate model, (b) high rate model with indenter. Green-Lagrange first principal strain in the global coordinate system.

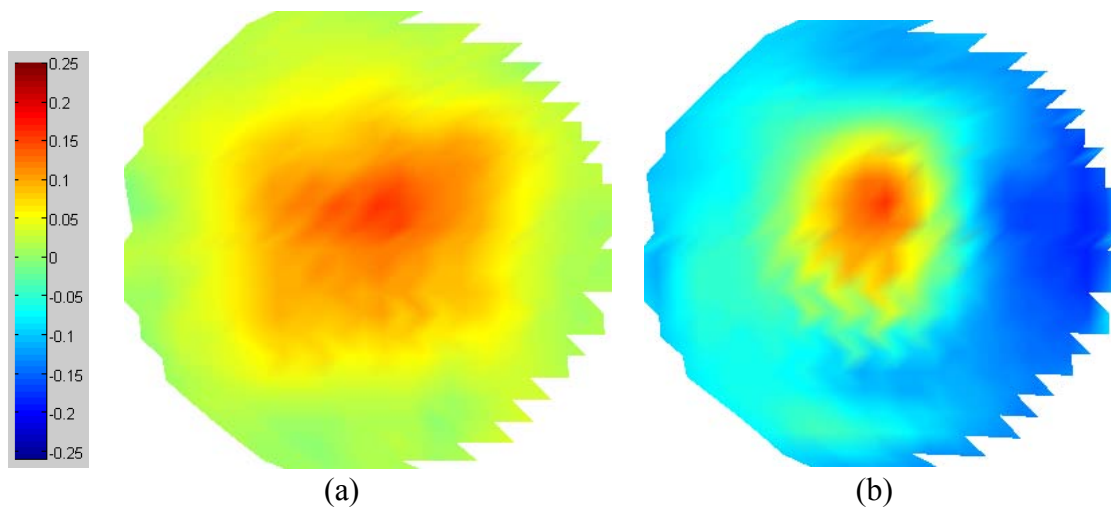
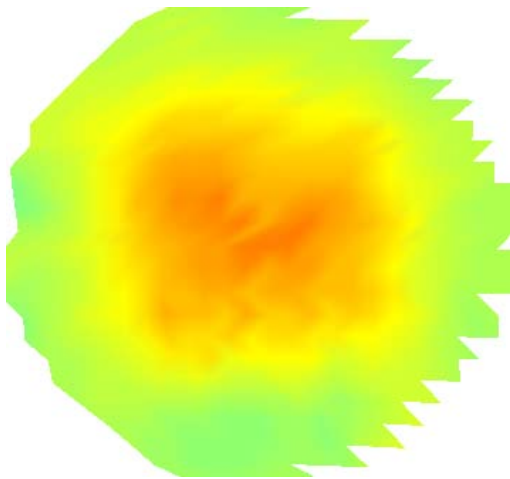
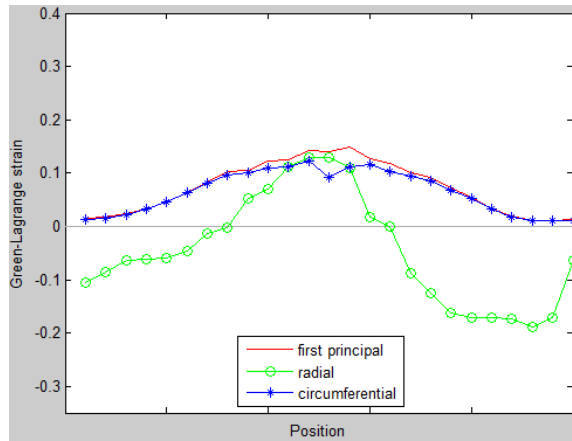


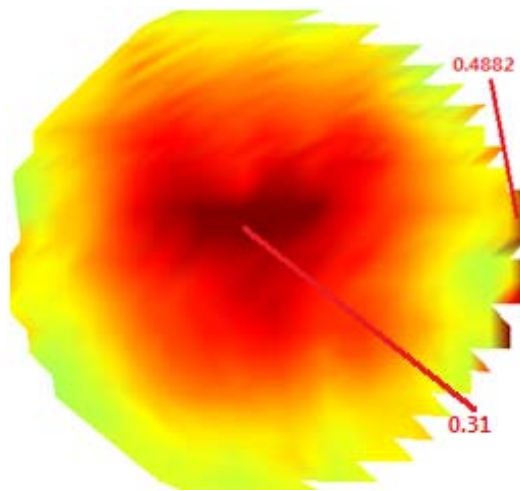
Figure 3.5. Green-Lagrange strain distribution – influence of rate : (a) first principal, (b) radial, (c) circumferential strains at 2.35 m/s, with (d) corresponding strain values along the diameter of the craniotomy, and (e) first principal, (f) radial, (g) circumferential strains at 7.05 m/s, with (h) corresponding strain values along the diameter of the craniotomy.



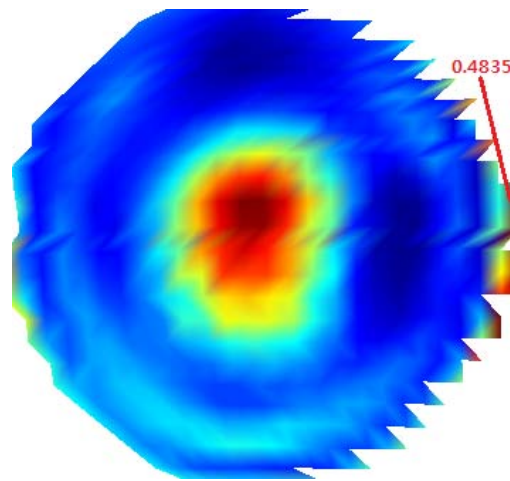
(c)



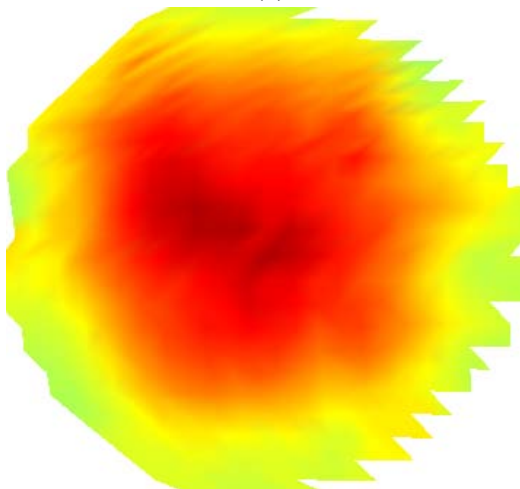
(d)



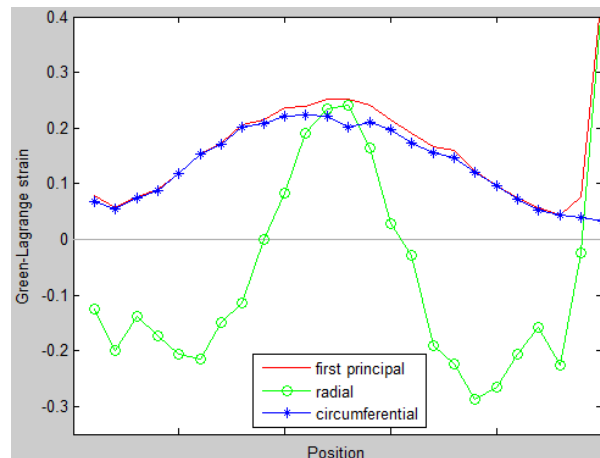
(e)



(f)



(g)



(h)

Figure 3.5 continued.

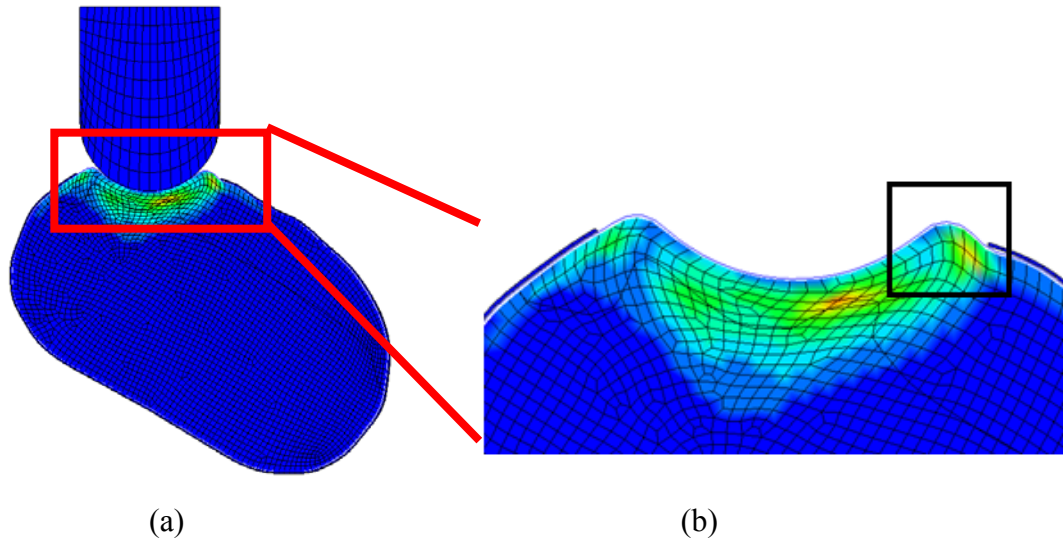


Figure 3.6. Green-Lagrange first principal strains in the global coordinate system. (a) Full and (b) zoomed-in coronal views of tissue deformation in the high rate model at the center of the impact site at maximum indentation with indenter removed. The black box in (b) highlights those elements in tension.

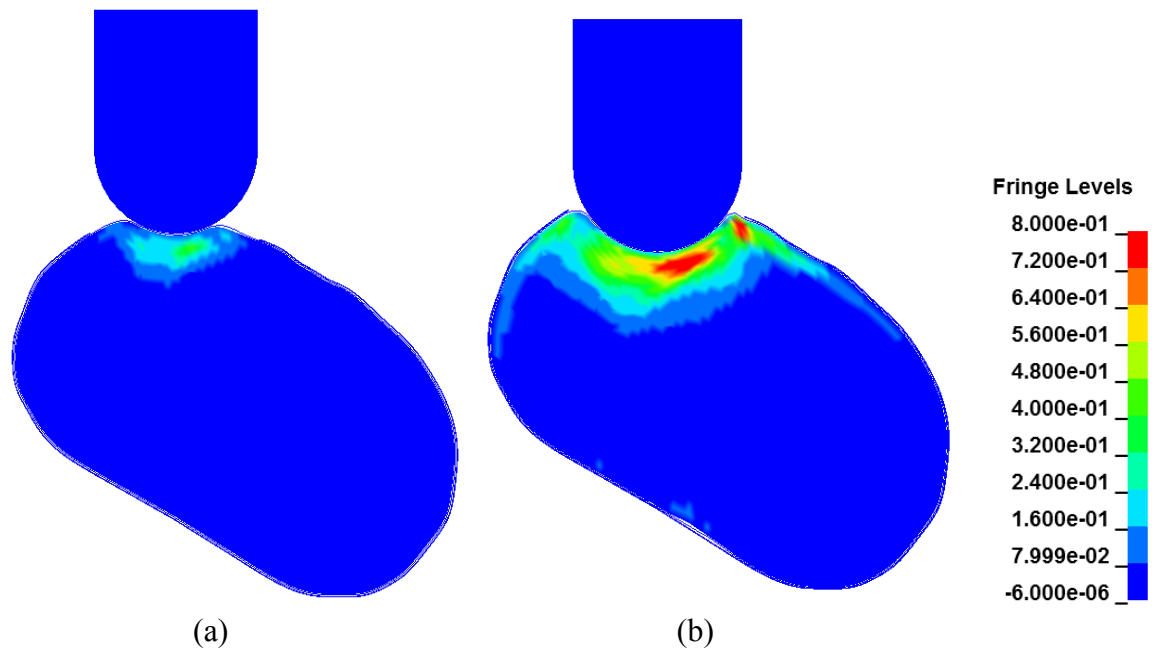


Figure 3.7. Cut view of (a) shallow depth model, (b) deep depth model with indenter. Green-Lagrange first principal strain in the global coordinate system.

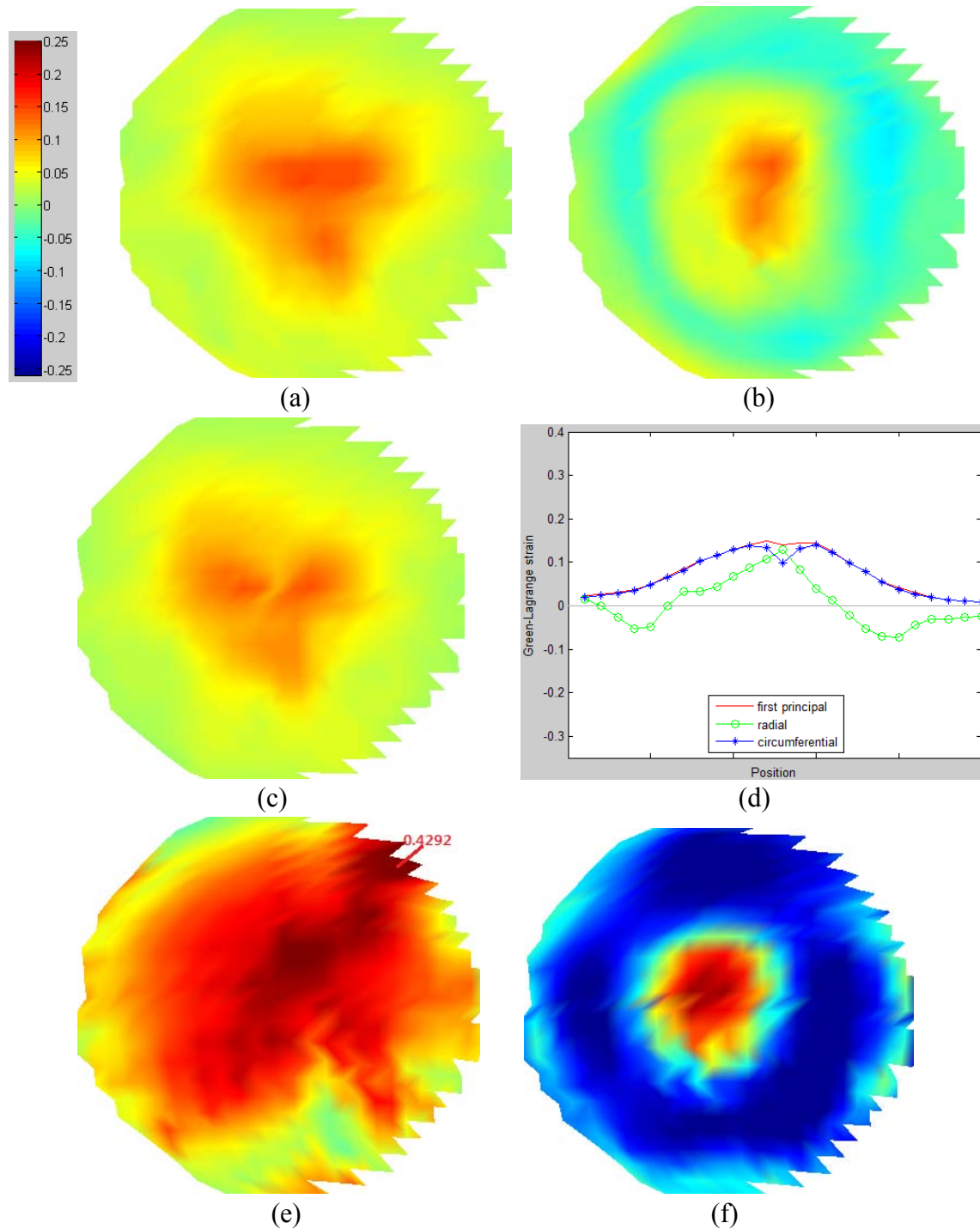


Figure 3.8. Green-Lagrange strain distribution – influence of depth : (a) first principal, (b) radial, (c) circumferential strains at 0.35 mm, with (d) corresponding strain values along the diameter of the craniotomy, and (e) first principal, (f) radial, (g) circumferential strains at 1.05 mm, with (h) corresponding strain values along the diameter of the craniotomy.

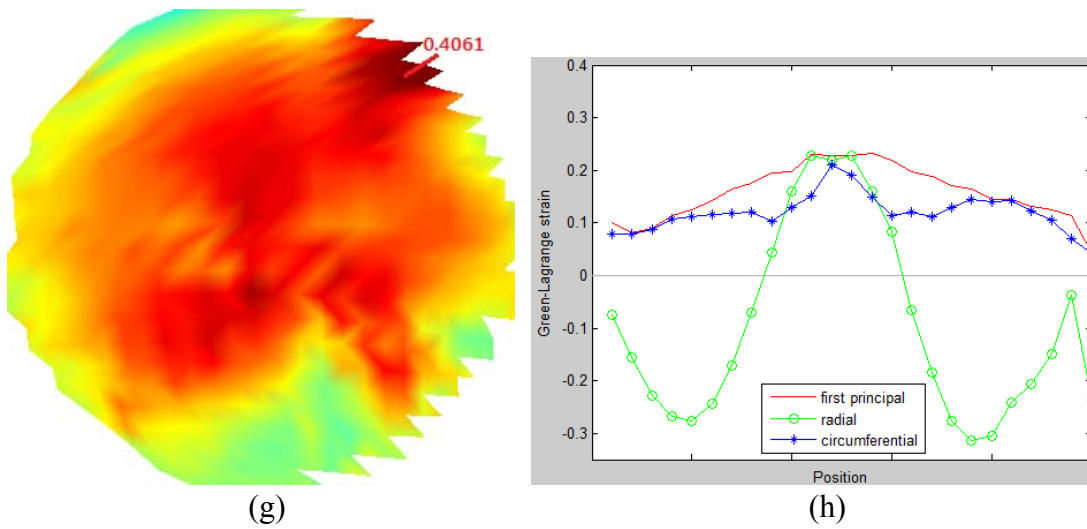


Figure 3.8 continued.

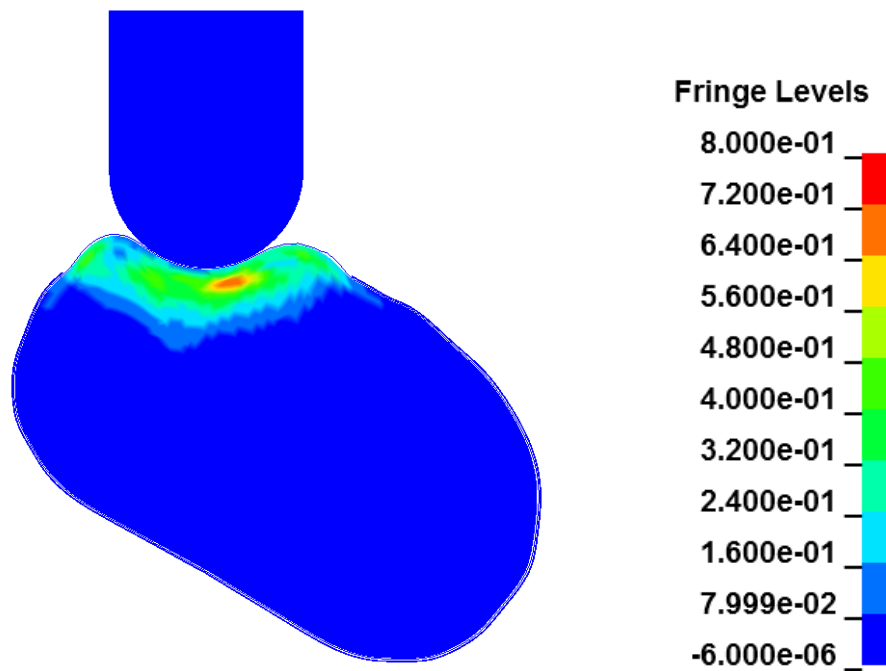


Figure 3.9. Cut view of craniotomy size model. Green-Lagrange first principal strain in the global coordinate system.

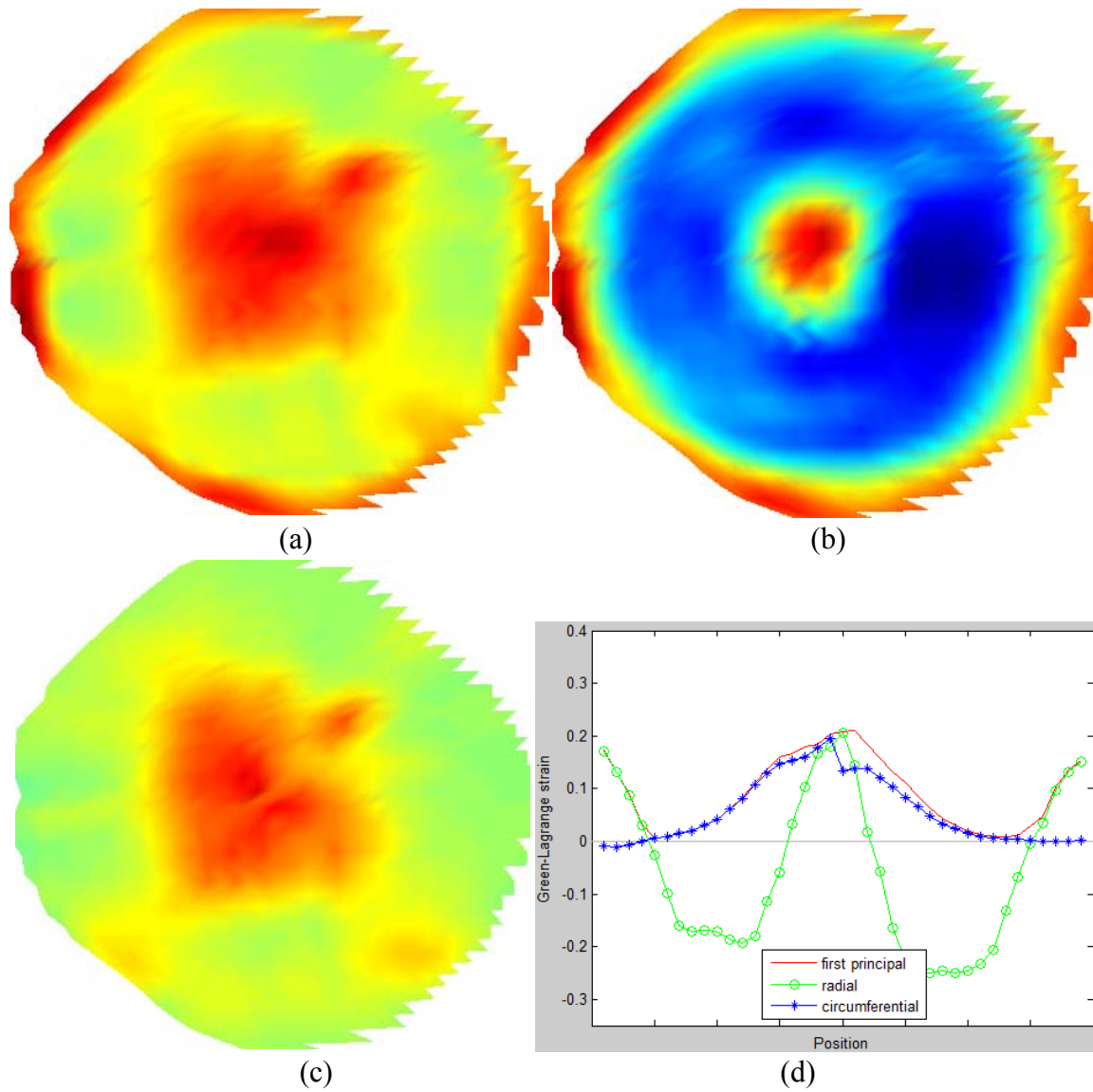


Figure 3.10. Green-Lagrange strain distribution on a large craniotomy model in the local coordinate system. (a) first principal strain, (b) radial strain, (c) circumferential strain, and (d) corresponding strain values along the diameter of the craniotomy.

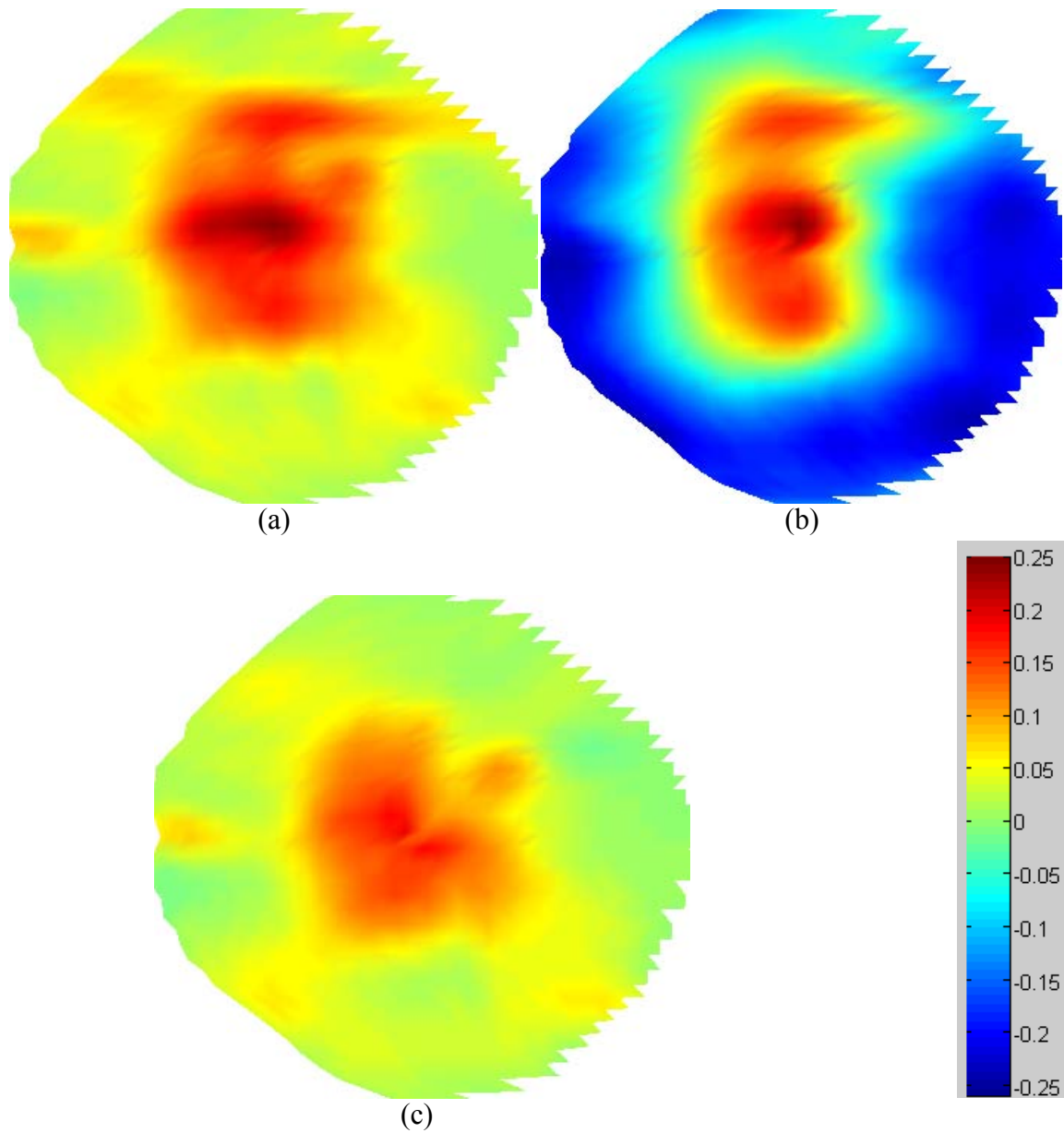


Figure 3.11. Green-Lagrange strain distribution on a large craniotomy model in the global coordinate system. (a) first principal strain, (b) radial strain, and (c) circumferential strain.

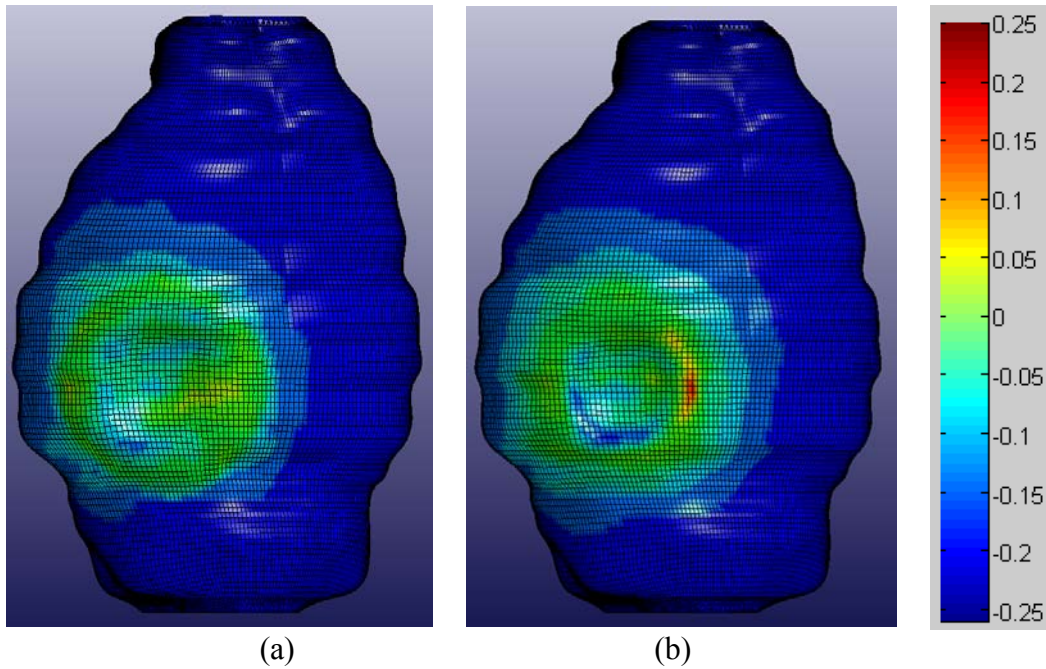


Figure 3.12. Green-Lagrange first principal strain distribution on the surface of the brain in global coordinate system from LS-Dyna (a) in a large craniotomy model, and (b) in baseline model.

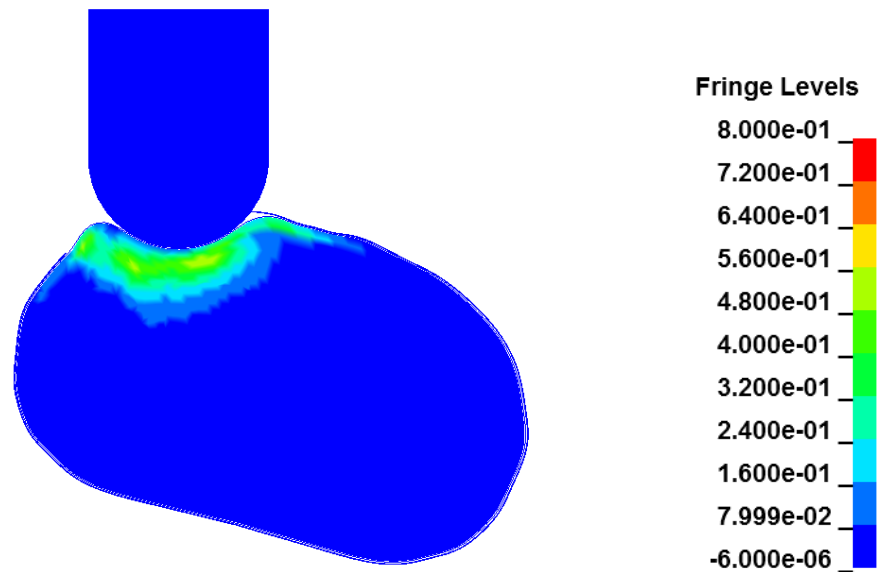


Figure 3.13. Cut view of indenter angle model. Green-Lagrange first principal strain in the global coordinate system.

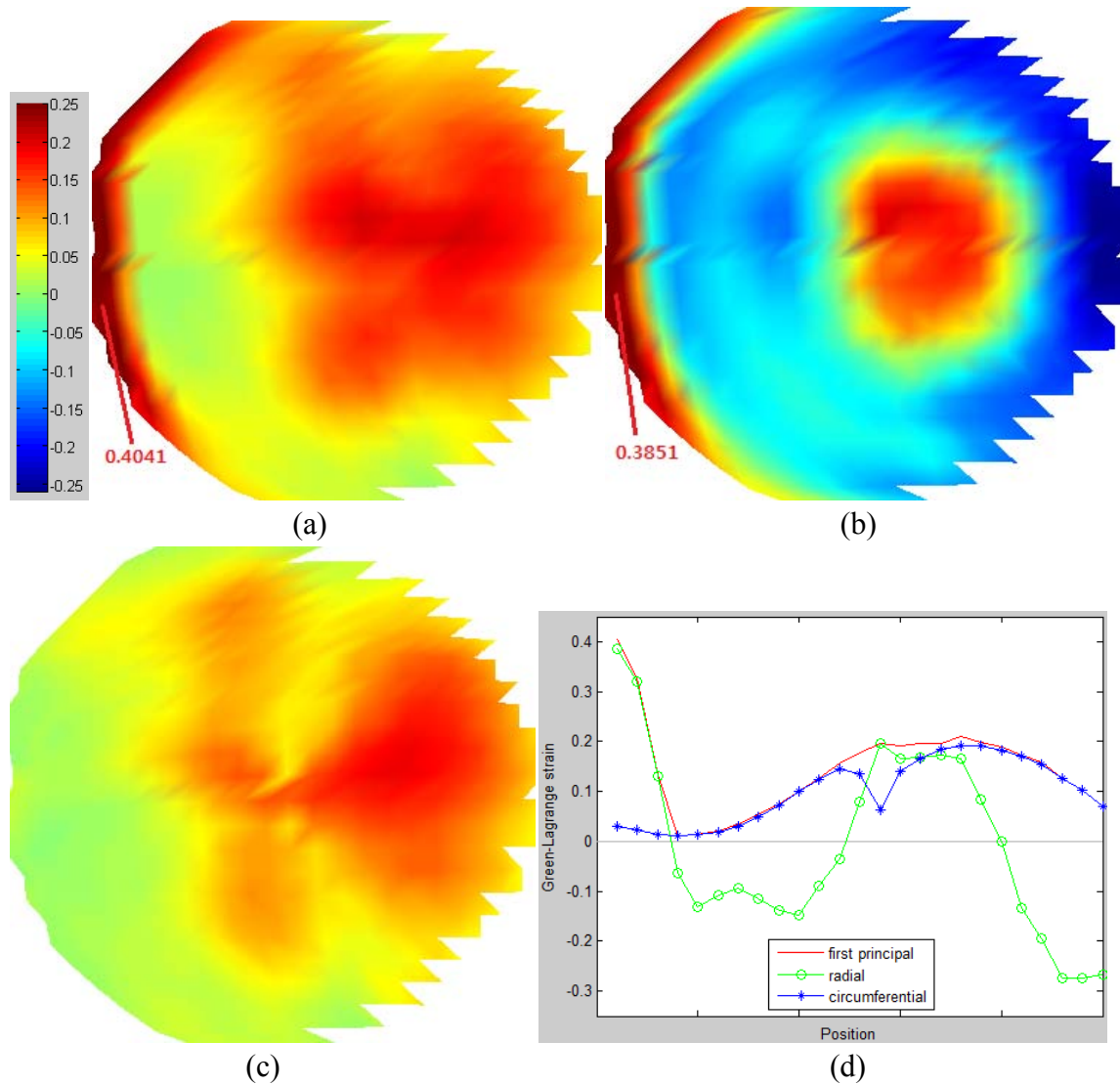


Figure 3.14. Green-Lagrange strain distribution for 15° variation in indenter angle (a) first principal strain, (b) radial strain, (c) circumferential strain, and (d) corresponding strain values along the diameter of the craniotomy.

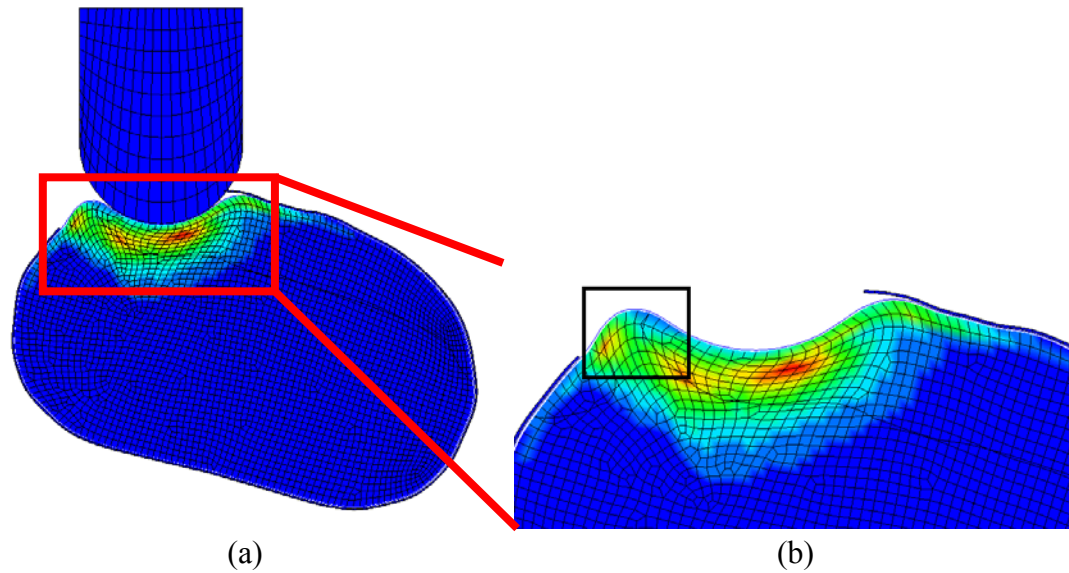


Figure 3.15. Green-Lagrange first principal strains in the local coordinate system. (a) Deformation on a coronal section of the brain tissue of indenter angle model at the center of the impact site at maximum indentation, (b) zoomed in view of (a) with indenter removed.

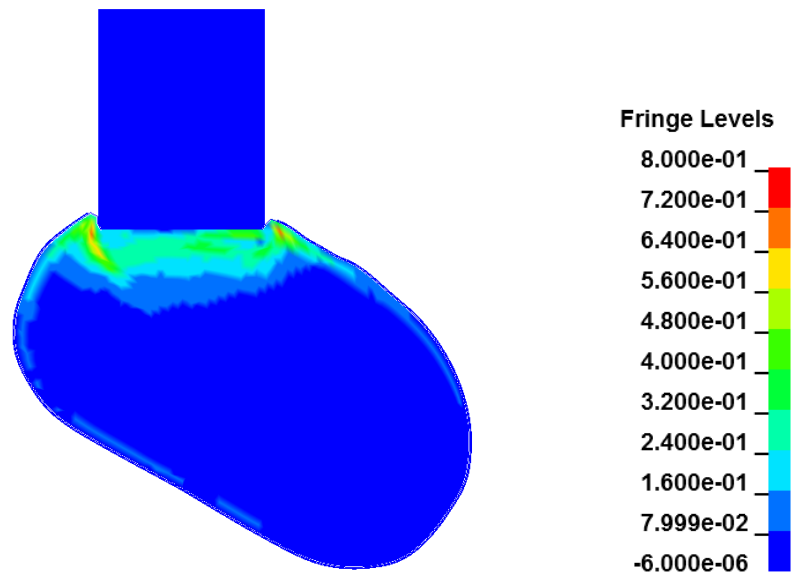


Figure 3.16. Cut view of indenter tip model. Green-Lagrange first principal strain in the global coordinate system.

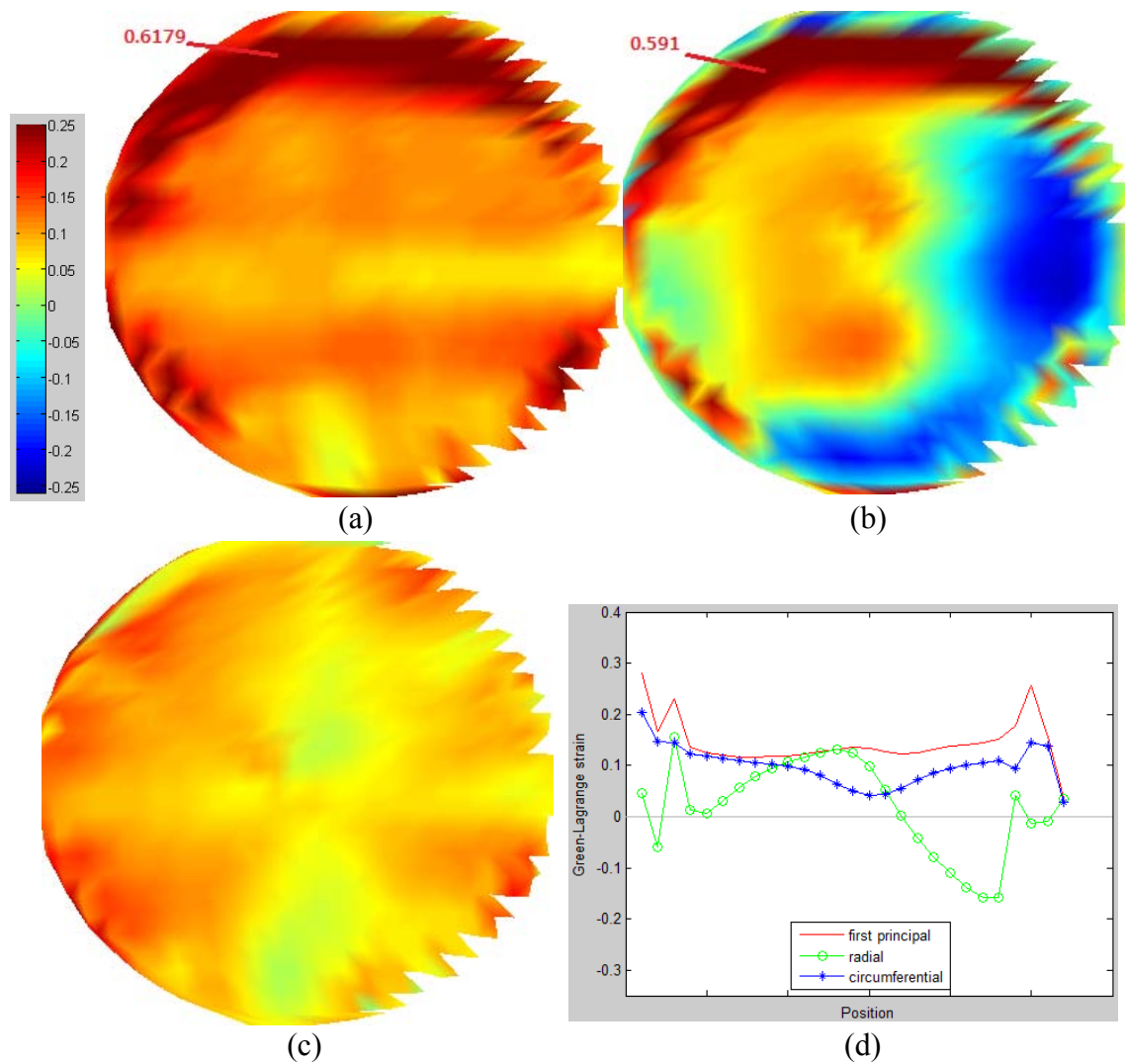


Figure 3.17. Green-Lagrange strain distribution. (a) first principal strain (b) radial strain, (c) circumferential strain with flat indenter tip, and (d) corresponding strain values along the diameter of the craniotomy.

CHAPTER 4

DISCUSSION

This study aimed to characterize strains experienced by blood vessels on the surface of the cerebral cortex during controlled cortical impact. To our knowledge, this is the first attempt to quantify deformations tangent to the brain surface during CCI. In the baseline model, circumferential strain is the primary contributor to principal strain over the whole craniotomy, while radial strain is high in the center but contributes little to principal strain away from the center. This suggests that vessels oriented circumferentially sustain greater strain than those that are radial. However, the maximum principal strain occurred in the radial direction at the center, and vessels oriented in the radial direction would sustain greater strain at the center. The maximum predicted strain on the surface in the baseline model is 0.2507. A blood vessel aligned in this direction would experience the same strain, which corresponds with an *in vivo* stretch of 1.22. Bell et al. [25] reported that failure stretch values relative to zero-load reference for human cerebral vessels range from 1.12– 1.35. Considering stretch relative to zero-load reference of 1.35 is equivalent to *in vivo* stretch of 1.1, we would almost always expect failure for such a vessel because *in vivo* stretch of 1.22 of the baseline model is greater than *in vivo* failure stretch of 1.1. All results of this research were compared to the human cerebral vessel failure thresholds since there is no significant difference between cerebral vessels of a human and a mouse, and the ultimate goal of this research is to study human vascular injury.

Maximum Green-Lagrange principal strain of low and high rate and small and large indentation models are 0.1564, 0.4882, 0.1483, and 0.4292, respectively. The magnitudes of strain change with the indentation rate and depth. Considering that the *in vivo* failure stretch of 1.1 is equivalent to Green-Lagrange strain of 0.105, even when rate and depth are considered at 50% of the values associated with the baseline model, the magnitudes are still above 0.105 strain, predicting that vessel failure would occur. As the rate and depth increase, stretch values also increase. The location of the maximum principal strain occurred at the center of the indentation at low rates and indentations, but this was not the case for high rates and indentations. In the latter cases, the maximum strains were found at the craniotomy boundary, and the exact locations vary depending on the shape of the brain surface. Therefore, it can be difficult for someone doing CCI experiments, especially those investigating vessel injuries. The vessels taken from the center of the indentation might not have experienced the maximum stretch. Therefore, it is recommended not to use the high rate and large indentation models since the low rate and small indentation models also can produce vessel injuries located at the center as well as the baseline model.

In the large craniotomy model, the maximum principal strain occurred at the center and also high strain was found at the craniotomy boundary. There is not a great difference between the maximum principal strain of the large craniotomy model of 0.2447 and that of the baseline model of 0.2507. The maximum strain of 0.2447 is greater than the failure strain of 0.105; therefore, vessel failure is expected. The strain magnitude and the maximum strain location at the craniotomy boundary can vary depending on the shape of the brain surface similar to the high rate and large indentation models. It is better not to

pursue CCI experiments with a larger craniotomy because it is difficult to find where the maximum strain occurs, and vessels taken from the brain might not have experienced the maximum stretch. The baseline loading condition would provide more reliable results since it is obvious that the maximum strain occurs at the center of the indentation with the baseline craniotomy.

The strain distribution of the indentation angle model is predictable. The strain concentration appeared opposite to the direction that the indenter came from. The maximum strain of 0.4041 located at the craniotomy boundary is greater than the failure strain of 0.105. Failure can be expected for a vessel with a different indentation angle. Since large strain can be found where the indenter struck directly and at the craniotomy boundary opposite to the direction that the indenter came from, it is not difficult to find vessels that experienced the maximum stretch. Varying indenter angle is helpful to investigate vessel injury with the CCI experiment.

The different tip shape model showed an asymmetrical strain contour plot due to the brain shape. The maximum strain appeared at the craniotomy boundary and some parts of the craniotomy boundary had higher strain than the other side. The location where the maximum strain occurred would vary depending on the surface shape of the brain. It is difficult to obtain consistent results with a flat tip. It is better not to pursue CCI experiments with a flat tip because it is difficult to find where the maximum strain occurs, and vessels taken from the brain might not have experienced the maximum stretch. The hemispherical tip would provide more reliable results since it is obvious that the maximum strain occurs at the center of the indentation.

Mao [7] reported results from his computational model of CCI in terms of global

coordinates. It is thus not possible to directly compare our findings, reported in the local coordinate system, to his. One thing we can qualitatively compare is the location of the maximum principal strain at a coronal section of the brain in the global coordinate system. Since Mao has the most similar model to this research, the results are qualitatively compared to those of Mao's, instead of others'. Figure 4.1(a) shows Mao's results [7] in the global coordinate system, and Figure 4.1(c) represents the result of this research in the global coordinate system. Even the indenter angle and tip shape of the models are different as shown in Figure 4.1(a) and (c), and the largest strains were observed near the area where the indenter and the brain made a contact initially, but at subsurface locations.

It is not possible to directly compare the results to the CCI experiment since it is difficult to observe what the tissue, including blood vessels, is experiencing. We can qualitatively compare with the CCI experiment by observing the location of damage on BBB. Yeo et al. [10] performed a CCI experiment and Figure 4.1(b) shows the IgG (red) around the penetrating blood vessels (green) after contusion injury, and there is a red area inside of the brain that ranged from about 0 to 400 microns. The distance from the surface to the maximum strain area in Figure 4.1(c) is about 250 microns. As these three figures of Figure 4.1 show the similar results in the global coordinate system, this first attempt to quantify deformations in the local coordinate system and the corresponding results in Chapter 3 are reliable.

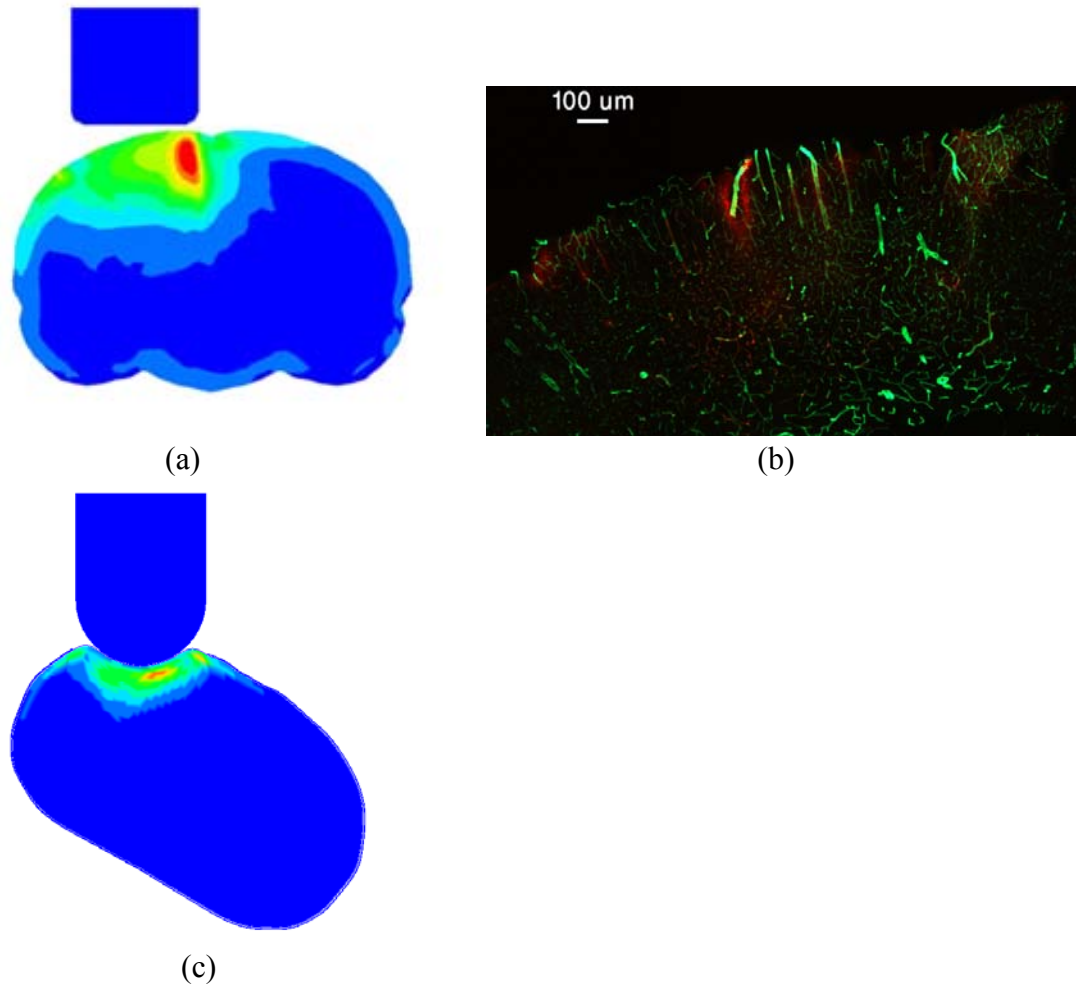


Figure 4.1. Qualitative comparison to previous researches. (a) Mao's contusion mechanism study [7], (b) distribution of IgG after contusion injury by Yeo et al. [10], (c) Green-Lagrange strain contour plot in the global coordinate system.

CHAPTER 5

CONCLUSION AND FUTURE WORK

The presented FE brain model helped characterize the CCI-induced strain field aligned with the surface of the cerebral cortex to study *in vivo* vascular injury. Results provide greater understanding of injury of blood vessels lying on the cortex. The brain geometry was built by digitizing the section images of the real mouse brain. Ventricles were excluded because ventricles did not have a big influence on the surface of the brain where we were interested. Strain distributions were investigated in the baseline model and with a variation of five different parameters: indentation rate, depth, craniotomy size, indentation angle, and indenter tip shape. Tip shape was the most influential parameter, producing the highest strain concentration on the surface of the brain. Indentation depth, rate, and angle also significantly influenced the strain distribution on the brain.

There were some limitations for this research. First, blood vessels were not included in the brain model. Blood vessels are stiffer than brain or meninges. Without relatively stiffer vessels lying on the brain, strains obtained from the model might be overestimated. Second, dura and skull are attached to each other in real life, and there is light bondage between them. Since the exact property of the bondage is not well known, surface contact was applied between them. Without considering the bondage, strains might be overestimated. The amount of the brain tissue extrusion between the indenter and the skull might decrease with the bondage. Third, shell elements were assigned for dura and

PAC, and in general, shell elements exhibit more stiff behavior than membrane. Since shell elements tend to have more resistance to bending, strains obtained from the model might be underestimated.

Future work could include explicit modeling of blood vessels on the surface of the brain, using the present results as a guide. Depending on the level of detail considered, this approach may require that only a portion of the brain be modeled. It would be difficult to include the indenter in such a microscale model. Alternatively, nodal coordinate histories from the current model could be used to provide boundary conditions. Using this microscale approach, a dense network of the blood vessels on the brain could be simulated. A similar approach could also be used to model a single blood vessel residing on the brain penetrating its surface. The FE brain model with cerebral vasculature will help predict *in vivo* vasculature injury and thresholds for contusion injury.

APPENDIX A

FINITE ELEMENT CODE

\$\$ Ls-dyna Input Deck Generated by HyperMesh Version : 12.0.0.85

\$\$ Generated using HyperMesh-Ls-dyna 971 Template Version : 12.0

*KEYWORD

*TITLE

\$# title

LS-DYNA keyword deck by LS-PrePost

*CONTROL_BULK_VISCOSITY

\$#	q1	q2	type	btype
	1.500000	0.060000	1	0

*CONTROL_ENERGY

\$#	hgen	rwen	slnten	rylen
	2	2	1	1

*CONTROL_TERMINATION

\$#	endtim	endcyc	dtmin	endeng	endmas
	0.300000	0	0.000	0.000	0.000

*CONTROL_TIMESTEP

\$#	dtinit	tssf	isdo	tslimt	dt2ms	lctm	erode	ms1st
	0.000	0.300000	0	0.000	0.000	0	0	0

\$#	dt2msf	dt2mslc	imscl	unused	unused	rmscl
	0.000	0	0			0.000

*DATABASE_BINARY_D3PLOT

```

$#      dt      lcdt      beam      npltc      psetid
      0.010000      0      0      0      0

$#  iopt
      0

*BOUNDARY_PRESCRIBED_MOTION_RIGID
$#      pid      dof      vad      lcid      sf      vid      death      birth
      1      2      2      1  1.000000      0      0.000      0.000

*BOUNDARY_SPC_NODE
$HMNAME LOADCOLS      1auto1
$HWCOLOR LOADCOLS      1      11
$#      nid      cid      dofz      dofz      dofz      dofz      dofz      dofz
      398708      0      1      1      1      1      1      1
      347630      0      1      0      1      1      1      1

*CONTACT_AUTOMATIC_SURFACE_TO_SURFACE_ID
$#      cid      title
      Odura / skull

$#      ssid      msid      sstyp      mstyp      sboxid      mboxid      spr      mpr
      5      6      3      3      0      0      0      0

$#      fs      fd      dc      vc      vdc      penchk      bt      dt
      0.200000  0.200000  0.000  0.000  0.000      0  0.000  0.000

$#      sfs      sfm      sst      mst      sfst      sfmt      fsf      vsf
      0.000  0.000  0.000  0.000  0.000  0.000  0.000  0.000

$#      soft      sofsc1      lcidab      maxpar      sbopt      depth      bsort      frefrq
      1      0.000      0      0.000  0.000      0      0      0

$#      penmax      thkopt      shlthk      snlog      isym      i2d3d      sldthk      sldstf
      0.000      0      0      0      0      0  0.000  0.000

$#      igap      ignodprfac/mpadtstif/mpar2      unused      unused      flangl      cid_rcf
      1      0  0.000  0.000      unused      unused      flangl      cid_rcf
      1      0  0.000  0.000      unused      unused      flangl      cid_rcf
      1      0  0.000  0.000      unused      unused      flangl      cid_rcf

```

*CONTACT_AUTOMATIC_SURFACE_TO_SURFACE_ID

\$#	cid								title
	2PAC / dura								
\$#	ssid	msid	sstyp	mstyp	sboxid	mboxid	spr	mpr	
	4	5	3	3	0	0	0	0	
\$#	fs	fd	dc	vc	vdc	penchk	bt	dt	
	0.200000	0.200000	0.000	0.000	0.000	0	0.000	0.000	
\$#	sfs	sfm	sst	mst	sfst	sfmt	fsf	vsf	
	0.000	0.000	0.000	0.000	0.000	0.000	0.000	0.000	
\$#	soft	sofscf	lcidab	maxpar	sbopt	depth	bsort	frcfreq	
	2	0.000	0	0.000	0.000	0	0	0	
\$#	penmax	thkopt	shlthk	snlog	isym	i2d3d	sldthk	sldstf	
	0.000	0	0	0	0	0	0.000	0.000	
\$#	igap	ignodprfac/mpadtstif/mpar2	unused	unused	flangl	cid_rcf			
	1	0	0.000	0.000		0.000	0		

*CONTACT_AUTOMATIC_SURFACE_TO_SURFACE_ID

\$#	cid								title
	3dura / piston								
\$#	ssid	msid	sstyp	mstyp	sboxid	mboxid	spr	mpr	
	5	1	3	3	0	0	0	0	
\$#	fs	fd	dc	vc	vdc	penchk	bt	dt	
	0.200000	0.200000	0.000	0.000	0.000	0	0.000	0.000	
\$#	sfs	sfm	sst	mst	sfst	sfmt	fsf	vsf	
	0.000	0.000	0.000	0.000	0.000	0.000	0.000	0.000	
\$#	soft	sofscf	lcidab	maxpar	sbopt	depth	bsort	frcfreq	
	2	0.000	0	0.000	0.000	0	0	0	
\$#	penmax	thkopt	shlthk	snlog	isym	i2d3d	sldthk	sldstf	
	0.000	0	0	0	0	0	0.000	0.000	

\$#	igap	ignodprfac/mpadtstif/mpar2	unused	unused	flangl	cid_rcf
	1	0	0.000	0.000		0.000
						0

*PART

\$# title

1 piston

\$#	pid	secid	mid	eosid	hgid	grav	adpopt	tmid
	1	3	3	0	0	0	0	0

*SECTION_SOLID_TITLE

solid

\$#	secid	elform	aet
	3	1	0

*MAT_RIGID_TITLE

rigid

\$#	mid	ro	e	pr	n	couple	m	alias
	3	7.8500E-6	200.00000	0.280000	0.000	0.000	0.000	

\$#	cmo	con1	con2
	0.000	0	0

\$#	lco or a1	a2	a3	v1	v2	v3
	0.000	0.000	0.000	0.000	0.000	0.000

*PART

\$# title

2 brain

\$#	pid	secid	mid	eosid	hgid	grav	adpopt	tmid
	2	3	4	0	0	0	0	0

*MAT_KELVIN-MAXWELL_VISCOELASTIC_TITLE

brain

\$#	mid	ro	bulk	g0	gi	dc	fo	so
	4	1.0400E-6	2.100000	1.7200E-6	5.1000E-7	20.000000	0.000	1.000000

*PART

\$# title

4 PAC

\$#	pid	secid	mid	eosid	hgid	grav	adpopt	tmid
	4	2	2	0	0	0	0	0

*SECTION_SHELL_TITLE

PAC

\$#	secid	elform	shrf	nip	propt	qr/irid	icomp	setyp
	2	1	0.000	0	1	0	0	1

\$#	t1	t2	t3	t4	nloc	marea	idof	edgset
	0.015000	0.015000	0.015000	0.015000	0.000	0.000	0.000	0

*MAT_ELASTIC_TITLE

PAC

\$#	mid	ro	e	pr	da	db	not used
	2	1.1300E-6	0.012500	0.450000	0.000	0.000	0

*PART

\$# title

5 dura

\$#	pid	secid	mid	eosid	hgid	grav	adpopt	tmid
	5	1	1	0	0	0	0	0

*SECTION_SHELL_TITLE

dura

\$#	secid	elform	shrf	nip	propt	qr/irid	icomp	setyp
	1	1	0.000	0	1	0	0	1

\$#	t1	t2	t3	t4	nloc	marea	idof	edgset
	0.020000	0.020000	0.020000	0.020000	0.000	0.000	0.000	0

*MAT_ELASTIC_TITLE

dura

\$#	mid	ro	e	pr	da	db	not used
	1	1.1300E-6	0.031500	0.450000	0.000	0.000	0

*PART

\$# title

6 skull

\$#	pid	secid	mid	eosid	hgid	grav	adpopt	tmid
	6	3	3	0	0	0	0	0

*DEFINE_CURVE

\$#	lcid	sidr	sfa	sfo	offa	offo	dattyp
	1	0	1.000000	1.000000	0.000	0.000	0

\$#	a1	o1
	0.000	0.000
	0.150000	0.700000
	0.300000	0.000

APPENDIX B

MATLAB CODE

```
for i=1:24

    load(sprintf('xx%d.csv',i));
    load(sprintf('xy%d.csv',i));
    load(sprintf('xz%d.csv',i));
    load(sprintf('zx%d.csv',i));
    load(sprintf('zy%d.csv',i));
    load(sprintf('zz%d.csv',i));
    load(sprintf('sx%d.csv',i));
    load(sprintf('sy%d.csv',i));
    load(sprintf('sz%d.csv',i));
    load(sprintf('sxy%d.csv',i));
    load(sprintf('syz%d.csv',i));
    load(sprintf('szx%d.csv',i));

end

X=[1;0;0];
Y=[0;1;0];
Z=[0;0;1];

xc = NaN(26,26);
zc = NaN(26,26);

prin_strain = NaN(26,26);
```

Cx = 2.2 ;

Cz = -3 ;

eR = NaN(26,26);

eC = NaN(26,26);

xr = NaN(26,26);

zr = NaN(26,26);

theta = NaN(26,26);

for j=1:24

% j = line numbers from the top to the bottom

% k = element numbers from the left

 sizetemp = eval(sprintf('size(xx%d)',j));

 sx=eval(sprintf('sx%d',j));

 sy=eval(sprintf('sy%d',j));

 sz=eval(sprintf('sz%d',j));

 sxy=eval(sprintf('sxy%d',j));

 syz=eval(sprintf('syz%d',j));

 szx=eval(sprintf('szx%d',j));

 xx=eval(sprintf('xx%d',j));

 xy=eval(sprintf('xy%d',j));

 xz=eval(sprintf('xz%d',j));

 zx=eval(sprintf('zx%d',j));

 zy=eval(sprintf('zy%d',j));

 zz=eval(sprintf('zz%d',j));

for k=1:(sizetemp(1,2)-1)

 x1_j_k = [(xx(16,k+1)-xx(16,k)) ; (xy(16,k+1)-xy(16,k)) ; (xz(16,k+1)-xz(16,k))];

 E_j_k = [sx(16,k),sxy(16,k),szx(16,k) ; sxy(16,k),sy(16,k),syz(16,k) ;

```

szx(16,k),syz(16,k),sz(16,k)];

z1_j_k = [ (zx(16,2*k)-zx(16,2*k-1)) ; (zy(16,2*k)-zy(16,2*k-1)) ; (zz(16,2*k)-zz(16,2*k-1)) ] ;

n_j_k = cross(x1_j_k,z1_j_k) / norm(cross(x1_j_k,z1_j_k));

z2_j_k = cross(n_j_k,(x1_j_k/norm(x1_j_k)));

Xp_j_k = (X - dot(X,n_j_k)*n_j_k) / norm(X - dot(X,n_j_k)*n_j_k);

Zp_j_k = (Z - dot(Z,n_j_k)*n_j_k) / norm(Z - dot(Z,n_j_k)*n_j_k);

n2_j_k = cross(Xp_j_k,Zp_j_k)/norm(cross(Xp_j_k,Zp_j_k));

R_j_k = [ dot(X,Xp_j_k), dot(X,n2_j_k), dot(X,Zp_j_k);
          dot(Y,Xp_j_k), dot(Y,n2_j_k), dot(Y,Zp_j_k);
          dot(Z,Xp_j_k), dot(Z,n2_j_k), dot(Z,Zp_j_k)];

e_j_k = transpose(R_j_k) * E_j_k * (R_j_k);

prin_strain_j_k = (e_j_k(1,1)+e_j_k(3,3))/2 + sqrt(((e_j_k(1,1)-e_j_k(3,3))/2)^2+e_j_k(1,3)^2);

% radial and circum strains

xr_j_k = (xx(16,k)+xx(16,k+1))/2 - Cx;

zr_j_k = (zz(16,2*k)+zz(16,2*k-1))/2 - Cz;

theta_j_k = atan2(zr_j_k,xr_j_k);

RY_j_k = [cos(-theta_j_k), 0, sin(-theta_j_k);
          0,          1,          0;
          -sin(-theta_j_k),0, cos(-theta_j_k)];

eRC_j_k = transpose(RY_j_k) * e_j_k * RY_j_k;

eval(sprintf('e_%d_%d =e_j_k;',j,k));

eval(sprintf('prin_strain_%d_%d = prin_strain_j_k;',j,k));

eval(sprintf('eRC_%d_%d =eRC_j_k;',j,k));

eval(sprintf('xr_%d_%d =xr_j_k;',j,k));

```

```

eval(sprintf('zr_%d_%d =zr_j_k;',j,k));
eval(sprintf('theta_%d_%d =theta_j_k;',j,k));

eX(j,k) = e_j_k(1,1);
eZ(j,k) = e_j_k(3,3);
xc(j,k) = xx(16,k);
zc(j,k) = xz(16,k);
prin_strain(j,k) = prin_strain_j_k;
eR(j,k) = eRC_j_k(1,1);
eC(j,k) = eRC_j_k(3,3);
end

clear sx sy sz xx xy xz zx zy zz sizetemp
end

figure(1);
pcolor(xc,zc,prin_strain);
set(gca,'CLim',[-0.2628,0.2507]);
colorbar;
title('1st Princial Strain');
shading interp;

figure(2);
pcolor(xc,zc,eR);
set(gca,'CLim',[-0.2628,0.2507]);
colorbar;
title('Radial strain');
shading interp;

```

```
figure(3);  
pcolor(xc,zc,eC);  
set(gca,'CLim',[-0.2628,0.2507]);  
colorbar;  
title('Circumferential strain');  
shading interp;
```

```
figure(4);  
plot(prin_strain(12,:));  
set(gca, 'XTickLabel', []);  
set(gca, 'XGrid', 'off');  
ylim([-0.2628,0.2507]);  
hy = graph2d.constantline(0, 'Color',[.7 .7 .7]);  
changedependvar(hy,'y');  
title('1st Princial Strain');
```

```
figure(5);  
plot(eR(12,:));  
set(gca, 'XTickLabel', []);  
set(gca, 'XGrid', 'off');  
ylim([-0.2628,0.2507]);  
hy = graph2d.constantline(0, 'Color',[.7 .7 .7]);  
changedependvar(hy,'y');  
title('radial');
```



```
figure(6);  
plot(eC(12,:));  
set(gca, 'XTickLabel', []);  
set(gca, 'XGrid', 'off');  
ylim([-0.2628,0.2507]);  
hy = graph2d.constantline(0, 'Color',[.7 .7 .7]);  
changedependvar(hy,'y');  
title('circumferencial');
```

REFERENCES

- [1] “Centers for Disease Control and Prevention.” <http://www.cdc.gov/injury//>.
- [2] Mauritz, W., Wilbacher, I., Majdan, M., Leitgeb, J., Janciak, I., Brazinova, A., and Rusnak, M., 2008, “Epidemiology, Treatment and Outcome of Patients After Severe Traumatic Brain Injury in European Regions with Different Economic Status,” *Eur. J. Pub. Health*, 18(6), pp. 575–580.
- [3] Finnie, J. W., and Blumbergs, P. C., 2002, “Traumatic Brain Injury,” *Vet. Pathol.*, 39(6), pp. 679–689.
- [4] Faul, M., Likang, X., Wald, M. M., and Coronado, V. G., 2010, “Traumatic Brain Injury in the United States: Emergency Department Visits, Hospitalizations and Deaths 2002-2006,” (Atlanta), Centers for Disease Control and Prevention, National Center for Injury Control and Prevention,.
- [5] Werner, C., and Engelhard, K., 2007, “Pathophysiology of Traumatic Brain Injury : A Review,” *Br. J. Anaesth.*, 99(1), pp. 4–9.
- [6] Finnie, J. W., 2001, “Animal Models of Traumatic Brain Injury: A Review,” *Aust. Vet. J.*, 79(9), pp. 628–633.
- [7] Mao, H., 2009, “Computational Analysis of In Vivo Brain Trauma,” Ph.D. thesis, Wayne State University, Detroit, MI.
- [8] King, A. I., Yang, K. H., Zhang, L., and Hardy, W., 2003, “Is Head Injury Caused by Linear or Angular Acceleration?,” in *IRCOBI Conference Proceedings*, Lisbon, Portugal.
- [9] Adams, J. H., Graham, D. I., Scott, G., Parker, L. S., and Doyle, D., 1980, “Brain Damage in Fatal Non-Missile Head Injury,” *J. Clin. Pathol.*, 33(12), pp. 1132–1145
- [10] Yeoh, S., Zentgraf, B., and Monson, K., 2012, “Injury to Penetrating Blood Vessels in Cerebral Contusion,” in *Proceedings of the ASME 2012 Summer Bioengineering Conference*, Fajardo, Puerto Rico, pp. 479–480.
- [11] Pena, A., Pickard, J. D., Stiller, D., Harris, N. G., and Schuhmann, M. U., 2005, “Brain Tissue Biomechanics in Cortical Contusion Injury: A Finite Element Analysis,” *Acta Neurochir.*, 95, pp. 333–336.

- [12] Engel, D. C., Mies, G., Terpolilli, N. A., Trabold, R., Loch, A., De Zeeuw, C. I., Weber, J. T., Maas, A. I. R., and Plesnila, N., 2008, "Changes of Cerebral Blood Flow during the Secondary Expansion of a Cortical Contusion Assessed by C-Iodoantipyrine Autoradiography in Mice Using a Non-Invasive Protocol," *J. Neurotrauma*, 25(7), pp. 739–753.
- [13] Chu, C. S., Lin, M. S., Huang, H. M., and Lee, M. C., 1994, "Finite Element Analysis of Cerebral Contusion," *J. Biomech.*, 27(2), pp.187–194.
- [14] Granger, D. N., and Granger, J., 2010, "Colloquium Series on Integrated Systems Physiology: from Molecule to Function to Disease," Morgan & Claypool Life Sciences, San Rafael, CA, pp. 5–10.
- [15] Bayly, P. V., Black, E. E., Pedersen, R. C., Leister, E. P., and Genin, G. M., 2006, "In Vivo Imaging of Rapid Deformation and Strain in an Animal Model of Traumatic Brain Injury," *J. Biomech.*, 39(6), pp. 1086–1095.
- [16] Shreiber, D. I., Bain, A. C., and Meaney, D. F., 1997, "In Vivo Thresholds for Mechanical Injury to the Blood-Brain Barrier," *Proc. Stapp Car Crash Conf.*, 41, pp. 277–291.
- [17] Levchakov, A., Linder-Ganz, E., Raghupathi, R., Margulies, S. S., and Gefen, A., 2006, "Computational Studies of Strain Exposures in Neonate and Mature Rat Brains during Closed Head Impact," *J. Neurotrauma*, 23(10), pp. 1570–1580.
- [18] Nolte, J., 2002, *The Human Brain: an Introduction to its Functional Anatomy: Fifth Edition*, Mosby, Maryland Heights, MO, pp. 98–117, Chap. 2–4.
- [19] Rosen, G. D., Williams, A. G., Capra, J. A., Connolly, M. T., Cruz, B., Lu, L., Airey, D. C., Kulkarni, K., and Williams, R. W., 2000, "The Mouse Brain Library @ www.mbl.org," http://www.mbl.org/atlas170/atlas170_frame.html
- [20] Tadepalli, S. C., Erdemir, A., Sett, S., and Cavanagh, P. R., 2010, "A Comparison of the Performance of Hexahedral and Tetrahedral Elements in Bone-Soft Tissue Finite Element Models," *Proceedings of the ASME 2010 Summer Bioengineering Conference*, Naples, FL, pp. 839–840.
- [21] Bonet, J., and Burton, A. J., 1998, "A Simple Average Nodal Pressure Tetrahedral Element for Incompressible and Nearly Incompressible Dynamic Explicit Applications," *Commun. Numer. Meth. En.*, 14(5), pp. 437–449.
- [22] Puso, M. A., and Solberg, J., 2006, "A Stabilized Nodally Integrated Tetrahedral," *Int. J. Numer. Meth. Eng.*, 67(6), pp.841–867.
- [23] Mathur, V., 2010, "Computational Modeling of Controlled Cortical Impact in a Mouse," Master's thesis, University of Utah, Salt Lake City, UT.
- [24] Livermore Software Technology Corporation, 1998, "LS-Dyna Theoretical Manual,"

Livermore, CA.

- [25] Bell, E. D., Kunjir, R. S., Monson, K. L., 2013, "Biaxial and failure properties of passive rat middle cerebral arteries," *J. Biome.*, 46(1), pp. 91–96.